國 立 交 通 大 學

光 電 工 程 學 系

博 士 論 文

可調單頻 Nd:$GdVO_4$ 雷射及其光譜應用

Tunable single frequency Nd:$GdVO_4$ laser and its spectroscopic applications

研 究 生: 施 能 謙

指導教授: 謝文峰 教授

施宙聰 教授

中華民國一零三年三月

可調單頻 Nd:$GdVO_4$ 雷射及其光譜應用

Tunable single frequency Nd:$GdVO_4$ laser and its spectroscopic applications

研 究 生: 施 能 謙　　Student: Nang-Chian Shie

指導教授: 謝文峰 教授　　Advisor: Dr. Wen-Feng Hsieh

施宙聰 教授　　Dr. Jow-Tsong Shy

國 立 交 通 大 學

光 電 工 程 學 系

博 士 論 文

A Dissertation

Submitted to Department of Photonics and Institute of Electro-Optical Engineering

College of Electrical and Computer Engineering

National Chiao Tung University

in Partial Fulfillment of the Requirements for the

Degree of Doctor of Philosophy

in

Electro-optical Engineering

March 2014

Hsinchu, Taiwan, Republic of China

中華民國一百零三年三月

可調單頻 Nd:$GdVO_4$ 雷射及其光譜應用

研究生：施能謙　　指導教授：謝文峰 教授
施宙聰 教授

國立交通大學光電工程學系博士班

摘要

本論文旨在以體積型布拉格光柵做為平凹共振腔輸出端反射鏡而建立中心波長 1070 nm 之單模 Nd:$GdVO_4$ 固態雷射。再經過週期性極化鈮酸鋰晶體產生二倍頻後，此雷射是銫原子宇稱性不守恆實驗中的極佳光源。銫原子宇稱性不守恆測量需有精密之原子理論計算，本論文利用此光源對銫原子 $6P_{3/2} \rightarrow 7S_{1/2}$ 能階躍遷進行精密頻率測量，測量結果可驗證原子結構理論計算的正確性。此光源也用於測量碘分子在 535 nm 附近之超精細譜線。

我們建立的單模 1070 nm Nd:$GdVO_4$ 固態雷射的輸出功率可達 300 mW。此雷射在輸出功率 200 mW 時之光束傳輸因子 M^2 約為 1.2，擴散角約為 0.37°。在輸出功率 100 mW 時以共振腔調控之單模頻率範圍達 5.1 GHz。我們以共焦式共振腔對此光源進行鎖頻，得到相對頻率穩定度為 7.58 kHz。此穩頻光源由光纖放大器提升功率後再經過週期性極化鈮酸鋰晶體，藉由非線性效應產生二倍頻得到 535 nm 光源。

Nd:$GdVO_4$ 雷射倍頻光源掃描碘分子在 535 nm 附近之 P(28) 30-0 超精細光譜，並針對其中 a_1, a_{10} 及 a_{15} 各超精細譜線進行絕對頻率量測。本論文利用飽和光譜三次諧波解調技術產生頻率誤差訊號，將 Nd:$GdVO_4$ 光源穩頻在碘分子光譜的超精細譜線上，當雷射光源穩頻在 a_1 譜線時之頻率穩定度在平均時間 10 秒時可達 3×10^{-12}。光頻梳測量雷射光源穩頻於超精細譜線的絕對頻率，絕對頻率測量結果續經壓力頻移量的修正後得到零壓力下的絕對頻率值。最後我們也針對 a_{10} 超精細譜線測量其壓力增寬效應及功率增寬效應。

中空陰極管中之鉈原子兩同位素 ^{203}Tl 及 ^{205}Tl $6P_{3/2} \rightarrow 7S_{1/2}$ 躍遷的飽和吸收光譜由 Nd:$GdVO_4$ 雷射倍頻光源利用波長調制三次諧波解調技術得到超精細光譜，並由此得到頻率誤差訊號來進行雷射穩頻。分析雷射穩頻後的頻率誤差訊號，得到頻率穩定度在 1 秒平均時間時可達 30 kHz，此穩頻光源將可做為鉈原子的雷射冷卻之用，也可用來研究鉈原子宇稱性不守恆。藉由精密波長儀測量穩頻光源之頻率得到鉈原子超精細譜線的絕對頻率，準確度達 30 MHz，經壓力頻移量的修正兩同位素的躍遷頻率之頻率重心的準確度可達 22 MHz，且推算出的同位素頻移量符合現知文獻資料。此鉈原子精密頻率測量結果將可做為鉈原子波動函數精確度的測試及檢驗基準。

Tunable single frequency Nd:$GdVO_4$ laser and its spectroscopic applications

Student: Nang-Chian Shie

Advisors: Dr. Wen-Feng Hsieh
Dr. Jow-Tsong Shy

Department of Photonics and Institute of Electro-Optical Engineering

National Chiao Tung University

Abstract

This thesis work developed a single frequency diode-pumped Nd:$GdVO_4$ laser at 1070 nm using a volume Bragg grating as the output coupler of a short plano-concave cavity. After second harmonic generation with a periodically-poled lithium niobate (PPLN), this laser is an excellent source for parity non-conservation (PNC) experiments using thallium atom. The accuracy of atomic theory which is needed to determine the thallium PNC motivated us to include the precise frequency measurement of the thallium $6P_{3/2} \rightarrow 7S_{1/2}$ transition as part of this thesis. The light source was also utilized realize the absolute frequency measurements of the hyperfine components of molecular iodine at 535 nm.

The developed 1070 nm single frequency Nd:$GdVO_4$ laser can achieve an output power of 300 mW. The beam propagation parameter M^2 at 200 mW was ~1.2, and the divergence angle was ~0.37°. The single frequency range with cavity length tuning was 5.1 GHz at 100 mW output power. We also locked the laser frequency to a confocal reference cavity and a relative stability of 7.58 kHz was achieved. After amplification of the fiber amplifier, the frequency stabilized 1070 nm laser passed through a PPLN to obtain a 535 nm light source by second harmonic generation.

The absolute frequency of the a_1, a_{10}, and a_{15} hyperfine components of molecular iodine P(28) 30-0 line at 535 nm were measured with the frequency doubled Nd:$GdVO_4$ laser. The frequency doubled 1070-nm Nd:$GdVO_4$ laser was frequency stabilized to a hyperfine component of I_2 using the saturation absorption spectroscopy and the third harmonic demodulation technique. The frequency stability of 3×10^{-12} was achieved at 10 second averaging time when its frequency was stabilized to the a_1 component. An optical frequency comb was used to measure its absolute frequency. The pressure shift was investigated to obtain the absolute frequency at zero pressure. The effect of pressure and power broadening of the a_{10} component were also investigated.

The saturated absorption spectrum of the $6P_{3/2} \rightarrow 7S_{1/2}$ transition of ^{203}Tl and ^{205}Tl in a hollow cathode lamp was observed with the frequency-doubled 1070 nm Nd:$GdVO_4$ laser. Similar to the iodine spectrum measurement, the third-derivative spectrum of the hyperfine components were obtained using the wavelength modulation spectroscopy and used to stabilize the laser frequency. Analysis of the error signal showed that the frequency stability reaches 30 kHz at 1 s averaging time. Such a frequency-stabilized light source at 535 nm can be used for laser cooling of thallium and for investigating the PNC effect in thallium. The absolute frequencies of hyperfine components were measured with an accuracy of 30 MHz using a precision wavelength meter. Including the pressure shift correction, the center of gravity of the transition frequency was determined to an accuracy of 22 MHz for both isotopes. Meanwhile, the isotope shift (IS) derived was in good agreement with earlier measurement. The precision measurements of thallium atomic structure can serve as the experimental constraints and benchmarks for the improvements of thallium wavefunction calculations.

誌謝

因緣際會下，很幸運地在博士班的學涯中有了謝文峰老師及施宙聰老師兩位共同指導教授，兩位老師有著不同的行事風範，卻有相同的研究熱忱以及同樣的教育熱情，在兩位老師的領導下感到收穫滿載，研究工作以及論文撰寫也在兩位老師共同指導下才得以完成，特此感謝。

也感謝賴暎杰老師、電物系陳永富老師、清大物理系劉怡維老師、中央大學物理系易台生老師、中央大學光電系鍾德元老師在百忙中撥冗擔任口試委員，並給予寶貴的意見與指正。

實驗室是個大家庭，彼此協助才得以解決許多實驗問題，在此感謝仕恩及君瑀在實驗工作上不遺餘力地支援，也感謝阿毛、小丁、佩凌、小花、老爹在實驗工作上的討論與幫忙，也感謝平時聊天聊是非的家瑜。實驗室的歡笑吵雜聲將是永遠的回憶。

感謝工研院給予在職進修，感謝工研院朱時梁博士提供此進修機會。

感謝好友吳龍暉博士，在我準備博士班資格考筆試期間出借居屋，也感謝陳豐榮學弟熱心陪讀，並賀豐榮學弟順利取得博士學位。

感謝學長王井煦博士，從大學時代一直走在前面帶領我，在這過程中不間斷地解惑與導正，尤其是聽我發牢騷，解悶氣。

感謝和南寺的道懌師父及諸師兄弟多年來持續地關懷。

要感謝的人太多了！ 真誠感謝過程中所有的貴人。在工作多年後進修博士班是一個大挑戰，感謝家人的支持，特別感謝我的另一半純芳無怨無悔地鼓勵與支持，讓我在工作、學業與家庭的多重考驗下得以完成此學程。

Table of Contents

List of Figures

List of Tables

Chapter 1
Introduction

1.1 Motivation

High precision measurements of the PNC effects and the permanent electric dipole moment (EDM) using atomic systems are promising in testing the standard model (SM) and searching for the new physics. Heavy atoms, such as cesium (Cs) and thallium (Tl), are adopted in the PNC and EDM experiments because these symmetry violation effects are enhanced by their large nuclei. However, in the atomic PNC measurement, an accurate theoretical calculation of atomic structure is needed for such test. In the case of Cs, an accurate PNC measurement of 0.35% accuracy combined with an accurate calculation of 0.5% accuracy leads to the most accurate result for the weak charge of cesium nucleus, which can be compared with the prediction of the SM [1, 2]. On the contrary, the 1.7% uncertainty PNC experiment in Tl system using $6P_{1/2} \rightarrow 6P_{3/2}$ transition [3, 4], combining with the 2.5% accuracy of Tl atomic theory, leads to a total uncertainty of 3.0% for the inferred weak charge of thallium nucleus. The Tl atom, which has only one unpaired electron, is one of the best candidates to measure the weak charge of nucleus. However, its atomic structure is more complicated than the alkalis and the accuracy of theoretical calculation is limited. Precision measurements of thallium atomic structure, such as the absolute transition energy, hyperfine splitting (HFS) and IS can serve as the experimental constraints and benchmarks for the improvements of theory.

On the other hand, the measurement of the electric dipole moment of atomic Tl [5] has been the most precise experiments to set the upper limit of electron's EDM for decades, until the recent improvement using the molecular YbF [6]. The implementation of laser cooling on atomic thallium, which produces slow intensive

atomic beam or ultracold sample, can offer great advantages for further reducing systematic uncertainties and increasing signal strength for the EDM experiment. A cooling scheme based on the metastable $6P_{3/2}$ state has been proposed and investigated [7]. It utilizes the $6P_{1/2} \leftrightarrow 6D_{5/2}$ transition, which has a high transition rate and can be considered as a nearly closed two-level cooling cycle. However, the difficulty of this scheme is the availability of high power 352 nm cooling UV laser source. An alternative approach is the two-color Λ type cooling scheme, which can be adapted to AIII group atoms and has been realized for cooling indium [8]. In atomic thallium, as the energy levels shown in Fig. 1-1, it involves the $6P_{1/2}$ - $7S_{1/2}$ - $6P_{3/2}$ transitions at 378 nm and 535 nm. The 378 nm laser causes an optical pumping effect to trap population

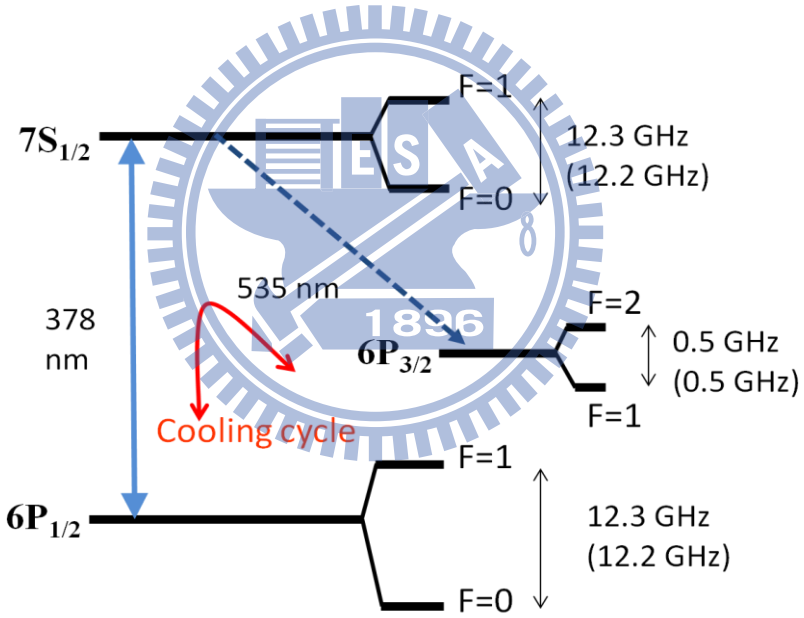

Fig. 1-1 Partial energy level of ^{205}Tl (^{203}Tl). Level shifts are not to scale.

in the $6P_{3/2}$ metastable state due to the large branch ratio of $7S_{1/2} \rightarrow 6P_{3/2}$ decay route (in comparison with $7S_{1/2} \rightarrow 6P_{1/2}$), then a long recovering time back to the $6P_{1/2}$ ground state. This implies a low effective laser cooling process. Another 535 nm laser is required to re-pump the population from $6P_{3/2}$ to $7S_{1/2}$ to form a closed cycling. Stable

and powerful laser sources of 378 nm and 535 nm are required to access the $6P_{1/2}$ - $7S_{1/2}$ - $6P_{3/2}$ transitions and to achieve laser cooling of thallium atom. For the 378 nm transition a laser source can be generated by frequency doubling the 755-nm light from a Ti:sapphire laser [9]. For the 535 nm transition, however, only dye laser system was available in the past. A reasonable method to acquire a 535 nm laser is to utilize frequency doubling from a 1070 nm laser. In addition to laser cooling, the 535 nm laser can be used in frequency measurement of the $6P_{3/2} \rightarrow 7S_{1/2}$ hyperfine transitions. Precision measurements of HFS and IS in thallium atomic structure will be used to guide the refinement and test the accuracy of the atomic theory calculation.

1.2 Achievements of Thesis

The main motivation of this work has been the development of a laser source for achieving the laser cooling of thallium atoms and frequency measurement of the $6P_{3/2} \rightarrow 7S_{1/2}$ hyperfine transitions. Fortunately, Neodymium-doped gadolinium vanadate (Nd:$GdVO_4$), a solid-state laser crystal, has an emission line around 1070 nm which can be used to obtain 535 nm by second harmonic generation [10], shown in Fig 1-2. The Nd-doped laser systems are well known for its 1063 nm lasing output wavelength and the 1070 nm emission band of the Nd laser crystal is weak and only 6 nm away from the main peak. The 1070 nm cross section is approximately five times smaller than that for the 1063 nm line. To obtain 1070 nm lasing with the Nd:$GdVO_4$ the competing transition channel at 1063 nm have to be suppressed. The 1070 nm band is too close to be separated from the 1064 nm band by a dielectric coated mirror. A volume Bragg grating (VBG) with many times narrower than the bandwidth achievable with multilayer coating is an ideal component to act as a wavelength selector [11]. VBGs offer an alternative approach for the wavelength selection and line narrowing in solid

state lasers [12, 13]. Using a VBG as an end mirror has been demonstrated great reduction of the laser output linewidth from few or few tenth of nm down to few pm or even single mode operation without a decrease in output power. Our aim was to achieve a 1070 nm single frequency diode-pumped Nd:$GdVO_4$ laser using a short plano-concave resonator in which a VBG serves the purpose of both the output coupler and the wavelength selector. The laser crystal was mounted on a piezoelectric transducer (PZT) for cavity length tuning. The frequency of the laser can be tuned coarsely by the VBG temperature and finely by the PZT voltage. When this proved to work as intended the single frequency laser was locked to the resonance peak of a confocal optical cavity to demonstrate its stability. Since the conversion efficiency attainable with a MgO doped periodically poled lithium niobate (MgO:PPLN) crystal is larger than with conventional crystals, a single pass PPLN frequency-doubling scheme was used to generate 535 nm light.

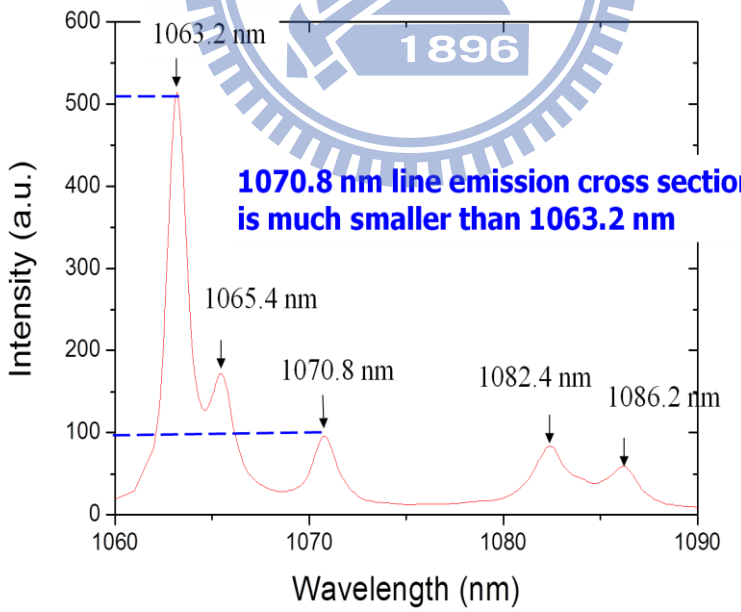

Fig. 1-2 Fluorescence spectrum of the laser crystal 0.5% at. Nd3+ doped GdVO4 at room temperature.

The tunable 535 nm laser was first applied to the absorption spectrum of molecular iodine. Third-harmonic demodulation technique was applied to analyze Doppler-free saturation spectrum to observe the hyperfine transitions of $^{127}I_2$ P(28) 30-0 line at 535 nm. The broad spectrum of molecular iodine has been widely used for optical wavelength reference or laser frequency stabilization in the visible and near-infrared region. Several of the iodine stabilized lasers are recommended as the wavelength standards by the Comité International des Poids et Mesures [14, 15]. The extensive precision measurements of iodine spectrum allow characterizing and calculating the iodine hyperfine structures [16]. The accuracy of the calculation depends on the high-precision transition frequencies measured by available stable laser sources. The Nd:$GdVO_4$ laser was stabilized to the a_1, a_{10}, and a_{15} hyperfine components and their absolute frequencies were measured by an optical frequency comb [17], respectively. Our results are useful for improving the theoretical calculation. After succeeding in the measurement of the iodine spectrum, the Nd laser proved a 535 nm light source for application in thallium spectrum.

The 535 nm laser was thus used to perform a precise measurement of the absolute frequencies of hyperfine components of the 535 nm $6P_{3/2} \rightarrow 7S_{1/2}$ transition for ^{203}Tl and ^{205}Tl. A hollow cathode lamp (HCL) was utilized to provide vapor of the atomic thallium at the metastable $6P_{3/2}$ state. To tune the laser wavelength to the thallium transition, the optogalvanic signal from the HCL was first detected to set the parameters of the laser system, e.g., the VBG and PPLN temperatures. The saturation spectroscopy was employed to resolve all the hyperfine transitions, and their absolute frequencies were measured using a precision wavelength meter [18]. We have achieved the frequency determination of the center gravity of the $6P_{3/2} \rightarrow 7S_{1/2}$ transition with accuracy better than 22MHz for both isotopes.

1.3 Organization of Thesis

This thesis is based on the works that have been reported in the published papers. After the introduction, Chapter 2 will introduce the basic background, including Standard Model, atomic parity non-conservation, properties of the volume Bragg grating and Nd:$GdVO_4$ solid state laser, for understanding the experiments and results. The experimental results achieved are presented in Chapter 3 to Chapter5. Chapter 3 covers the background and experiment of the developed solid state laser, where a 1070 nm Nd:$GdVO_4$ laser have been constructed with a volume Bragg grating as an output coupler. The experimental results of the absolute frequency measurements of the molecular iodine hyperfine transitions at 535 nm are presented in Chapter 4, where the 535 nm light source is the second harmonic generation of the amplified 1070 nm laser which goes through a PPLN. Chapter 5 presents the precise frequency measurements of the hyperfine transitions of thallium with the developed 535 nm light source, where a hollow cathode lamp provides as the thallium vapor cell. Each chapter has its own brief introduction and a summary of its contents. Finally a summary of this thesis and future works are given in Chapter 6.

Chapter 2

Basic Background

2.1 Parity Nonconservation and Thallium

2.1.1 Standard Model

The Standard Model (SM) of particle physics summarizes the present state knowledge of particles and their interactions. It is a quantum based theory using quantum chromodynamics to describe strong interactions and the electroweak theory to unify weak and electromagnetic interactions. The gravity is not included in the SM. The SM theory proposes that these interactions result from exchange of force carrier particles called gauge bosons. The strong interactions of quarks are thought to be mediated by massless gluons. And the electroweak theory claims that the interactions between leptons (electron, muon, tau, neutrinos) and spin 1/2 quarks (up, down, top, bottom, charm, strange) are all mediated by four spin 1 bosons: the photon (γ), the neutral boson (Z_0), and the charged bosons (W^+ and W^-). The photons mediate electromagnetic interaction, and the W and Z bosons mediate the weak interactions. There are two types of weak interaction. If a charged boson (W^+ or W^-) is mediated, the interaction is called charged-current interaction, and is responsible for the beta decay phenomenon. If a neutral boson (Z_0) is mediated, the interaction is called neutral current interaction. The Z_0 boson mass has been determined from the experiment at LEP to be 91.1876 ± 0.0021 GeV [19]. And, in the same way that an electric charge of a particle responses to an electromagnetic force, each particle and atomic nuclei have a weak charge Q_w which characterizes the weak force's effect. SM is the most successful theory of particle physics to date. It provides a precise description of the observed phenomena and has been consistent with nearly all experimental results. Despite this great success, even more precise experiments are needed to continue testing the predictions of the SM as any deviation would imply a sign on new physics.

2.1.2 Atomic Parity Non-conversation

Atomic PNC experiments have been important tests of the SM of electroweak interactions because they are sensitive to the electroweak interaction at low energy, determining the bound state of the electron in an atom. Atomic PNC experiments provide an important complement to the accelerator based high energy experiments and search for the new physics beyond the SM. In an atomic system, the interactions between electron and nucleus are ongoing and the electromagnetic interactions dominate through mediated photons. Meanwhile the weak interactions through mediated Z_0 boson exist in the presence of the relative huge electromagnetic interactions, perturbing the wavefunction of the electron by as much as one part in 10^{10}. The amplitude of the weak interaction must be measured under the interference of the electromagnetic interaction. The Z_0 boson, however, has a parity non-conserving trait. That is, the weak interaction violates parity symmetry, while the electromagnetic interaction does not. An observable parity violating effect in an atomic system can only be interpreted by the weak interaction. Precise atomic PNC experiments can be used to measure the weak charge Qw of the nucleus, which determines the strength of electroweak interaction, and test the electroweak theory.

The coupling between electron and nucleon may be determined experimentally by observing the PNC in the electron-nucleon interaction. The electroweak theory describes the electroweak transition amplitude as the sum of two different electron-nucleon contributions (Fig. 2-1): an electromagnetic one of amplitude A_{em} and a weak one of amplitude A_w,

$$A = A_w + A_{em}. \tag{2.1}$$

The transition rate is proportional to:

$$|A|^2 = |A_w|^2 + |A_{em}|^2 + 2\,\mathrm{Re}(A_w A_{em}^*). \tag{2.2}$$

The first term is of negligible magnitude and can be ignored. The second term is the dominant term. The third term is the interference term. The interference term can be experimentally distinguished as it changes sign under a parity transformation. If a difference in rates between two coordinate system of opposite handedness is observed, a parity violating asymmetry (A_{pv}) is proportional to the ratio of weak and electromagnetic amplitudes [20-22]

$$A_{PV} = \frac{\sigma_+ - \sigma_-}{\sigma_+ + \sigma_-} \approx \frac{A_w}{A_{em}} \approx \frac{G_F Q^2}{4\pi\alpha} \approx \frac{Q^2}{M_Z^2}, \tag{2.3}$$

where G_F is Fermi coupling constant, α is fine structure constant, and Q is momentum transfer. An asymmetry as large as 10^{-4} has been observed in the SLAC polarized electron experiment operating at $Q^2 \sim (1\text{GeV})^2$ [21]. In an atomic system, $Q^2 \sim (m_e\alpha)^2$, the asymmetry is expected to be of the order of 10^{-14}. In 1959, Zeldovich who predicted the optical activity of atomic media due to possible weak neutral currents [23] demonstrated the first proposals concerning effects of a weak electron-nucleon interaction in atoms with stable nuclei. Zeldovich realized the effect would be

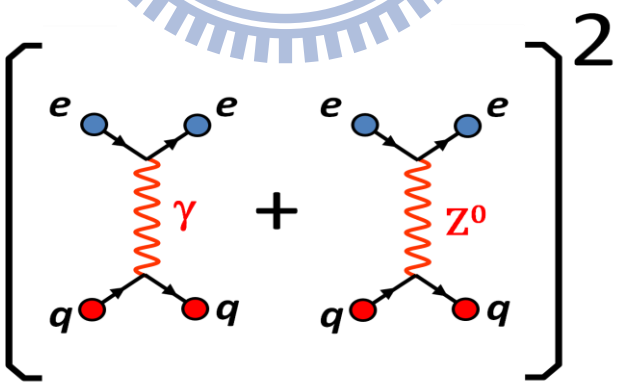

Fig. 2-1 Electrons in an atom interact with the nucleus through the electromagnetic force and weak force. The electromagnetic force is mediated by massless photons (γ). The weak force is mediated by Z_0 bosons.

immeasurably small at that time. However, the atomic PNC can be enhanced by several mechanisms. In 1974, M.A. Bouchiat and C. Bouchiat demonstrated that the strength of the atomic PNC scales with the cube of atomic number, the so-called Z^3 law [24]. Since then, it thus possible to test the atomic PNC effects in heavy atoms.

The parity-violating parts of the weak force between electrons and nucleons in an atom can be separated into two groups according to the dependence on the nuclear spin: nuclear spin dependent effects (NSD-PV) and nuclear spin independent effects (NSI-PV). The spin independent effects are much easier to measure since they are proportional to the number of nucleons, while NSD-PV effects, which include Z boson exchange between electrons and nucleons, and the nuclear anapole moment**,** have a net contribution only from the unpaired nucleons—of which there is typically only one. Consequently, the NSI-PVs dominate atomic PNC, whereas NSD-PVs contribute small corrections.

In the non-relativistic limit, the NSI-PV can be written as [25],

$$H_{PV}^{(NSI)} = \frac{G_F}{2\sqrt{2}} Q_w (\psi_e^{+} \gamma_5 \psi_e) \delta(r), \qquad (2.4)$$

where G_F is the weak coupling constant, Q_w is the weak nuclear charge, γ_5 is the Dirac matrix and $\delta(r)$ is the nucleon density function. In the SM, the nuclear charge

$$Q_w = -N + (1 - 4\sin^2 \theta_w) Z \approx -N, \qquad (2.5)$$

where N is the neutron number, Z is the proton number, and θ_w, the weak mixing angle, is given to lowest order accuracy by $\sin^2(\theta_w)=0.23$. The relation between Q_w and the PNC amplitude, E_{PNC}, can be represented as [26]

$$E_{PNC} = kQ_w, \qquad (2.6)$$

where k is an atomic-structure factor that can be computed from the atomic wavefunctions. The size of E_{PNC} is determined not only by the weak nuclear charge, but

also the electron probability density inside the nucleus. To interpret a PNC measurement as a measurement of Q_w requires an accurate atomic calculation. Precise measurements of the parameters such as the hyperfine structure and lifetime are helpful in improving the wavefunction calculation. With the atomic-structure calculations of k, an atomic PNC measurement can determine an experimental value of the weak charge. Any deviation of the SM predicted weak charge from the experimental weak charge will indicate a new physics.

2.1.3 Observations of Atomic Parity Nonconservation

Optical rotation and Stark interference are so far the only two different types of experimental measurements of atomic PNC. Optical rotations have been measured in atomic bismuth [27], lead [28], thallium [3, 4] and samarium [29]. In Stark inference experiments the atomic PNC can be measured by observing its interference with a Stark-induced electric dipole (E1) transition amplitude. The E1 transitions between atomic states of the same parity are strictly forbidden by QED. The Stark interference atomic PNC measurements have been performed on atomic cesium [1], thallium [30], and ytterbium [31]. In the case of Cs, a PNC measurement of 0.35% accuracy combined with a calculation of 0.5% accuracy leads to the most accurate result for the weak charge of cesium nucleus, which can be compared with the prediction of the SM [1, 2]. On the contrary, the 1.7% uncertainty of the PNC experiment in the Tl system using the $6P_{1/2} \rightarrow 6P_{3/2}$ transition [3, 4], combining with the 2.5% accuracy of Tl atomic theory, leads to a total uncertainty of 3.0% for the weak charge of thallium nucleus. The Tl atom, which has only one unpaired electron, is one of the best candidates to measure the weak charge of nucleus. However, its atomic structure is more complicated than the alkali metals and the accuracy of theoretical calculation is limited. Precision

measurements of thallium atomic structure, such as the absolute transition energy, HFS and IS can serve as the experimental constraints and benchmarks for the improvements of theory calculation. Our motivation for measuring the hyperfine structure and IS in thallium atom is to guide the refinement and to test the accuracy of the atomic theory calculation for the short-range electron wavefunction.

2.1.3 Thallium Structure

The thallium atom of atomic number 81 is a lead-like metal with a bright, freshly cut surface. It is soft and can be cut with a knife. After exposure to air an oxide layer forms quickly on surface. The water soluble thallium is highly toxic.

High atomic number makes Tl one of the best candidates to measure the weak charge of nucleus because of the Z^3 law [24]. The Tl electron configuration is $[Xe]4f^{14}\ 5d^{10}\ 6s^2\ 6p^1$, which has only one unpaired electron outside the S-state. Thallium has two stable isotopes, ^{205}Tl ~70.5% and ^{203}Tl~29.5%. Each Tl isotope has nuclear spin 1/2. This tells us that each fine structure state splits into two hyperfine states. A ground stat $6P_{1/2}$ electron has a greater probability of being found near the nucleus. A partial energy level diagram is shown in Fig. 2-2.

However, Tl with three valence electrons has a more complicated atomic structure compared with Cs, which has only one valance electron. The large correlations between three-valence electrons cannot be accurately calculated using many-body perturbation theory (MBPT) [35]. Several new theoretical approaches have been developed for such atoms, for example, MBPT combined with configuration interaction and MBPT combined with coupled-cluster [36]. Precision measurements of thallium atomic structure, such as the absolute transition energy, HFS and IS can provide cross-checks for the new theory.

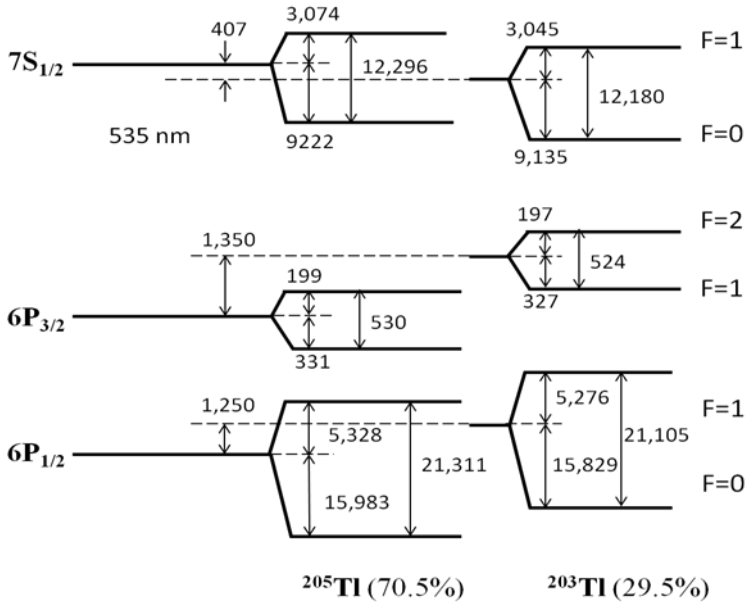

Fig. 2-2 Partial energy-level diagram of ^{203}Tl and ^{205}Tl with the HFSs and isotope level shifts in the unit of MHz. Energy levels are not to scale. [9] [32-34].

Early literatures have reported precise HFS measurements with uncertainties less than 1 kHz for both $6P_{1/2}$ and $6P_{3/2}$ states using microwave magnetic resonance techniques in the 1950s [32, 33]. Recently precise measurements of the absolute transition frequency and the HFS of the $6P_{1/2} \rightarrow 7S_{1/2}$ transition have been reported [9]. However, no precise measurements have been carried out for the $6P_{3/2} \rightarrow 7S_{1/2}$ transition at 535 nm up to now. This motivated us to measure the hyperfine structure of Tl transition $6P_{3/2} \rightarrow 7S_{1/2}$ using our developed single frequency Nd:$GdVO_4$ laser.

2.2 Volume Bragg Gratings

2.2.1 Properties of Volume Bragg Grating

VBG is a periodic phase grating recorded in a bulk material. Based on a linear

photosensitivity photo-thermo-refractive (PTR) glasses are the most successful material used to manufacture a high efficiency VBG. The PTR is a silicate glass doped with cerium, silver, and fluorine. After UV-exposure with a holographic technique and thermal development the precipitation of a minor crystalline phase results in a holographic phase pattern throughout the whole glass volume.

The PTR VBGs provide extremely narrow spectral selectivity down to 20 pm, good narrow angular selectivity down to 100 μrad, high absolute diffractive efficiency (above 99.9%), and thermally stability of 400℃ [37]. PTR VBG is mechanically, chemically and thermally stable. The damage threshold is close to that of the typical silicate glass. It has a laser damage threshold of 40 J/cm^2 for 8 ns pulses, and tolerance to CW laser radiation in the near IR region up to several tens of kilowatts per square centimeter. By changing the temperature of VBG, the central reflection wavelength can be tuned by about 10 pm/K around 1μ m due to thermal expansion of PTR glass. The PTR properties [37]:

- Photosensitivity ranges from 280 to 350 nm
- Transparency from 350 to 2700 nm
- Absorption in the near IR region below 0.0001 cm-1
- Refractive index 1.49
- Abbe number 60
- Photo-induced refractive index increment up to 1200 ppm
- Spatial frequencies from 0 (zero) to 10,000 mm-1
- Phase pattern cannot be erased by any type of optical or ionizing radiation

2.2.2 Volume Bragg Grating Applications in Lasers

Both reflecting and transmitting Bragg grating can be developed in the PTR glass.

These unique features make VBG ideal for working as intracavity wavelength selectors or resonator couplers in various types of lasers, depending on designed properties. VBGs offer an alternative approach for the wavelength selection and line narrowing in solid state lasers [12]. Its excellent wavelength selectivity has been demonstrated with laser diodes [38, 39], solid state lasers [12-13, 40-48], optical parametric oscillators [49-52] and fiber lasers [53-56]. Transversely chirped VBG has also been used for the wavelength tuning to obtain tunable solid-state laser [57] and OPO [58]. The VBG can also be used as a high power high-density beam combiner [59]. Thorough reviews of the prosperities and applications were given in refs. [60-64].

2.2.3 Diffraction Analysis for a Reflecting Volume Bragg grating

A theory which is based on a coupled-wave analysis for plane waves incident on a VBG was first presented by Kogelnik [65]. The PTR VBG consists of a sinusoidally varying refractive index modulation with period Λ according to $n = n_0 + n_1 \sin(2\pi x/\Lambda)$, where the modulation n_1 is up to 10^{-3} in magnitude. Assume a plane wave incident on the grating with an angle θ and wavelength λ. The reflected wavelength by Bragg condition is expressed as

$$\lambda_B = 2n_0\Lambda\cos\theta_0, \tag{2.7}$$

where θ_0 is the incident angle at Bragg condition. For each grating period of a reflecting VBG, there is the maximum wavelength $\lambda_B^{\max}$, which corresponds to normal incidence at $\theta_0 = 0$,

$$\lambda_B^{\max} = 2n_0\Lambda. \tag{2.8}$$

The beam incident on a reflecting VBG with wavelength exceeding $\lambda_B^{\max}$ cannot be diffracted by this particular grating at any conditions of excitation. The beam with

shorter wavelengths incident at larger angles can be reflected by a Bragg mirror. The total power reflectivity at the plane $x = 0$ can be expressed as [63]

$$R = \frac{\kappa'^2 \sinh^2(\sqrt{\kappa'^2 - \delta^2}\, d)}{\kappa'^2 \cosh^2(\sqrt{\kappa'^2 - \delta^2}\, d) - \delta^2}, \tag{2.9}$$

where the grating thickness d, wavevector mismatch $\delta = 2\pi n_0(\lambda^{-1} - \lambda_B^{-1})$ and $\kappa' = \frac{\pi n_1}{\lambda \cos\theta}$. The phase of the reflection is given by

$$\varphi(\delta) = \arctan\left(\frac{\delta}{\sqrt{\kappa'^2 - \delta^2}} \tanh(\sqrt{\kappa'^2 - \delta^2})\right) + m\pi, \tag{2.10}$$

where m is an integer. m should be altered at the reflectivity zero points to give the phase continuity. The peak diffraction efficiency is at $\delta = 0$,

$$R_{\max} = \tanh^2(\kappa' d) = \tanh^2\left(\frac{\pi n_1 d}{\lambda_B \cos\theta}\right) = \tanh^2\left(\frac{\pi n_1 d}{2 n_0 \Lambda \cos\theta_0 \cos\theta}\right) \tag{2.11}$$

The zero-to-zero bandwidth of the reflection is defined as the distance between the two zeros closest to the peak to get a simple expression for the VBG bandwidth. The zero-to-zero bandwidth for the wavelength at constant incidence angle is

$$\Delta\lambda = \lambda_B \sqrt{\frac{n_1^2}{n_0^2 \cos^4\theta_0} + \frac{4\Lambda^2}{d^2}}, \tag{2.12}$$

where θ_0 is the incident angle at Bragg condition. The bandwidth and the reflectivity can be varied independently by varying parameters n_1 and d. At a constant wavelength, the zero-to-zero angular bandwidths for normal incidence are

$$\Delta\theta_n = 2\sqrt{\frac{\Delta\lambda}{\lambda_B}}, \tag{2.13}$$

and for oblique incidence

$$\Delta\theta_0 = 2\frac{1}{\tan\theta_0}\frac{\Delta\lambda}{\lambda_B}. \tag{2.14}$$

The temperature dependence of the central wavelength for normal incidence is

$$\frac{\partial \lambda_B}{\partial T} = \lambda_B \left(\frac{1}{n} \frac{\partial n}{\partial T} + \alpha \right), \tag{2.15}$$

where α is the thermal expansion of the glass material. The measured temperature dependences of wavelength change are 23.4 pm/℃ at 2479 nm [66] and 10 pm/℃ at 1024 nm [67]. As the nonlinear refractive index of PTR [68] the wavelength change with temperature is not directly proportional to the Bragg wavelength. The temperature tuning capability can be used to thermally control laser wavelength. The VBG thermal tuning capability for a solid-state laser was demonstrated in a Ti:sapphire laser system. [12]

When a thick VBG is used as one of the mirrors of a short Fabry-Perot cavity, the grating's physical length can be a substantial part of the total cavity length. The effective round trip distance can be calculated from the phase acquired from a reflection of a Bragg grating. The effective cavity length L_{cav} is deuced to be [13]

$$2L_{cav} = \frac{R^{1/2}}{\operatorname{arctanh} R^{1/2}} d \,. \tag{2.16}$$

If the incident light is a finite beam with a varying distribution in the transverse direction, the behavior of VBG is different from the plane wave. Reflectivity and spectral bandwidth are dependent on incidence angle and beam waist. Also, the transverse beam profile of a finite incident beam on the grating will be altered in both transmission and reflection, for the different angular components of the incident beam experience different reflectivities. Theory and experiments of finite beams in reflective VBG have been presented in ref. [63] and [69]. In ref. [69], the diffraction efficiency for finite beam incidence was demonstrated and shown in Fig. 2-3. With the finite beam behavior, the VBG can be used as a spatial filter, since higher order transverse modes have a broader angular spectrum. And, adjusting the beam incident waist can cause the Gaussian mode to be reflected completely, but the higher order

ones only partially. Thus the VBG can be used as a mode filter to limit the number of transverse modes in a laser cavity.

The reflection spectrum of our PTR VBG made from OptiGrate is shown in Fig. 2-4 [from 70]. The peak reflectivity is centered at 1069.8 nm with full width at half maximum (FWHM) about 0.356 nm. The peak reflectivity is larger than 0.99 according to OptiGrate.

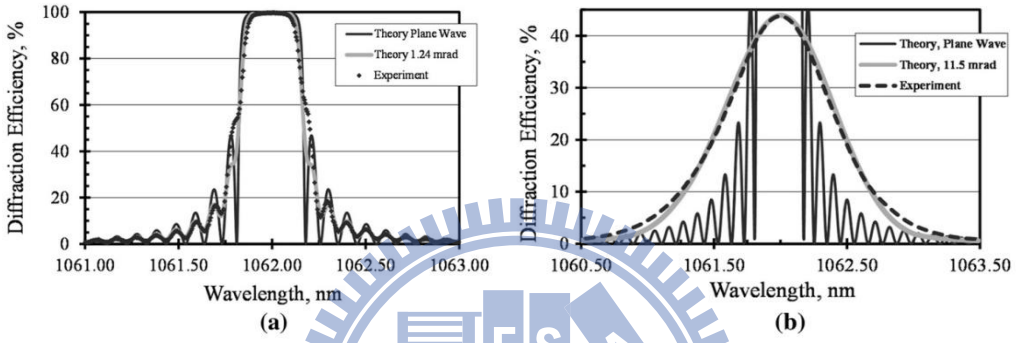

Fig. 2-3 Comparison of Modeling with experimental diffraction efficiency of finite beam in reflective volume Bragg grating (a) 1.24 mrad beam divergence; (b) 23 mrad beam divergence [from ref. 70]

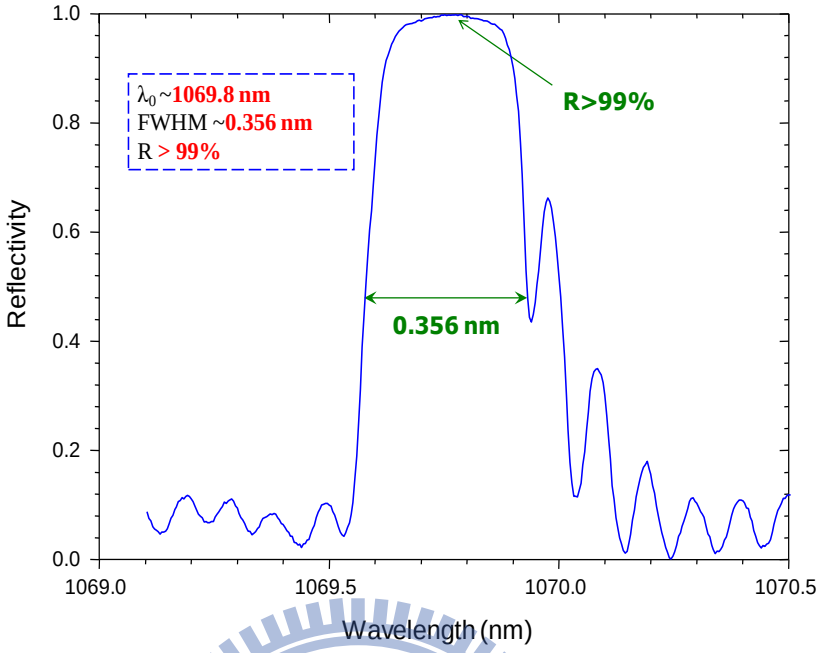

Fig. 2-4 Reflection spectrum of the VBG is centered at about 1069.8 nm with FWHM 0.356 nm and peak reflectivity larger than 99%. [from ref. 70, 71]

2.3 Nd:$GdVO_4$ Solid State Laser

A laser is a light source based on light amplification by stimulated emission of radiation. Every laser system essentially is constructed from three basic components: a gain medium, a pump, and a cavity, shown schematically in Fig. 2-5. A gain medium placed between a pair of optically parallel and highly reflecting mirrors with one of them partially transmitting. An energy source pumps gain medium that has appropriate energy levels, where population inversion is obtained. The cavity provides a resonant amplification via the stimulated emission after the population inversion. The gain media may be solid, liquid, or gas. The basics of the laser theory can be found in photonics textbooks.

In this thesis, the gain medium is lanthanide ions doped in a crystal or glass host

and the pump source is a laser diode, the so called diode pump solid-state lasers. The laser cavity feedback was constructed by a dielectric mirrors and a spectrally selective volume Bragg grating.

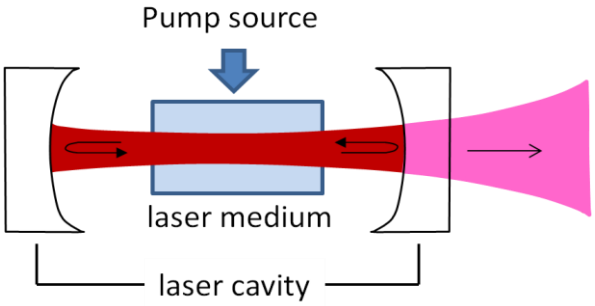

Fig. 2-5 Schematic diagram of a typical laser, showing the three major components: a gain medium, a pump and a resonant cavity by the mirrors.

2.3.1 Laser Gain Medium Nd:$GdVO_4$

The laser crystal is one of the most important components of a solid-state laser, and it can determine the efficiency of the laser. Nd:$GdVO_4$, which is similar to Nd:YVO_4 crystal and Nd:$GdVO_4$ crystal, is an excellent laser crystal for diode pumped laser used as a four-level laser pumped at 808 nm. It is common lasing at 1064 nm. Nd:$GdVO_4$ have higher optical efficiency than Nd: YAG crystals and better thermal conductivity and higher power output than Nd: YVO_4 crystals, so they are a good choice for high power output diode pumped solid state laser. Also, Nd:$GdVO_4$ can be operated at linear polarization. These properties make Nd:$GdVO_4$ a good laser material for many laser applications. Table 2-1 shows the comparison of Nd-doped solid state materials. Figure 2-6 shows a simplified energy level diagram of the $^4F_{3/2}\rightarrow{}^4I_{11/2}$ manifolds. The close view of $^4F_{3/2}\rightarrow{}^4I_{11/2}$ transitions manifold has been shown in Fig. 1-2. It was acquired by an Agilent 70950B optical spectrum analyzer when the crystal is pumped by an optical power of 2.3 W at 808 nm [70]. Nd:$GdVO_4$

has an emission line at about 1070 nm, which was used to generate 535 nm laser by second harmonic generation in this thesis work.

Table 2-1 Comparison of Nd-doped solid state material [96, 97]

	$Nd:GdVO_4$	$Nd:YVO_4$	Nd:YAG
Crystal Structure	Tetragonal	Tetragonal	Cubic
Pump Wavelength	808.5 nm	808.7 nm	807.5 nm
Lasing Wavelengths	912.6 nm, 1063.1 nm, 1341.3 nm	914nm, 1064 nm, 1342 nm	1064 nm
Thermal Conductivity (W/m/K)	11.7 <110>	‖C: 5.23 ^C: 5.10	14 11
Stimulated Emission Cross-Section (cm^{-2} , @1064 nm)	$7.60x10^{-19}$	$25.0x10^{-19}$ $15.6x10^{-19}$	$2.8x10^{-19}$
Fluorescent Lifetime (ms @ 808 nm)	95	90	230
Absorption Coefficient (cm^{-1})	74 (E‖C) 10 (E⊥C)	40 (E‖C) 10 (E⊥C)	11
Polarized Laser Emission	parallel to optic axis	parallel to optic axis	Unpolarized
Diode Pumped Optical to Optical Efficiency	> 60%	> 60%	

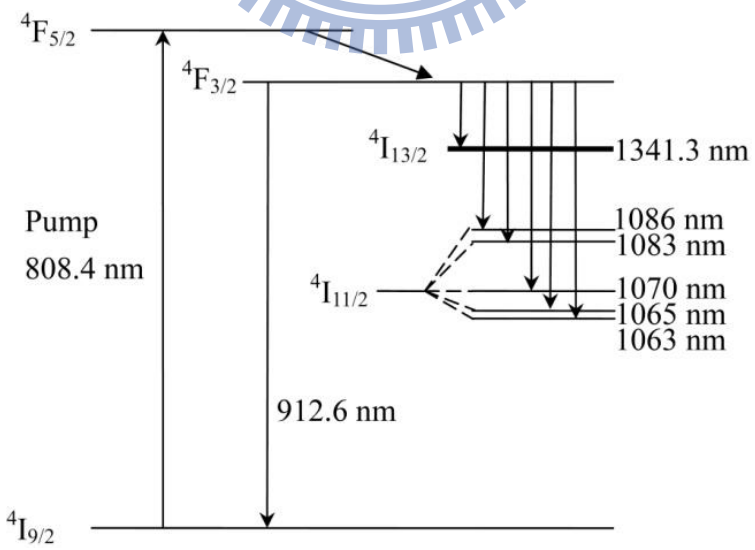

Fig. 2-6 A simplified energy level diagram of the $^4F_{3/2} \rightarrow {}^4I_{11/2}$ manifolds [70]

2.3.2 Wavelength Selection

The Nd-doped laser systems are well known for its 1064 nm lasing output wavelength, which belongs to the transition between $^4F_{3/2}$ and one of the Stark levels of $^4I_{11/2}$. The lasing actions between $^4F_{3/2}$ and other Stark levels within $^4I_{11/2}$ manifold are strongly suppressed because of smaller stimulated emission cross sections [72] and close spacing between these Stark levels. Therefore, to achieve 1070.8 nm laser wavelengths of Nd:$GdVO_4$, 1063.2 nm emission has to be suppressed.

Several methods have been commonly used for mode selection and spectral narrowing of a broad band laser toward achieving a single longitudinal mode laser, for example, by introducing an etalon, birefringent plate, surface grating, and (or) prisms in the cavity. The intracavity filters, however, typically induce substantial losses at the desired wavelength to raise the threshold and to lower the slope efficiency. At the same time dispersive elements such as prisms or diffraction gratings necessitates the use of a longer cavity. In most cases multiple selective elements must be used to achieve single frequency laser, and introduce added complexity.

A possible scheme is using a highly spectrally selective cavity mirror. A 1083 nm laser has been achieved and reported using a specially coated dielectric mirror with high reflectivity at 1082.6 nm and lower reflectivity around 1060 nm [10]. However, such a specifically dielectrically coated mirror is impractical for those even closer lines such as 1065 and 1070 nm since these two peaks are too close for coating design and the mirror reflectivity will be too high at 1082.6 nm which makes the 1082.6 nm line dominate in such a system instead of 1070.8 nm.

As a better alternative a highly spectrally selective cavity output coupler can be realized with a new type of robust optical element, a VBG recorded in PTR glass.

Owing to its narrow spectral and angular selectivity, VBG offers an advantage of at least 1 order of magnitude in the bandwidth use over a conventional surface diffraction grating. Using a VBG as an end mirror has been demonstrated great reduction of the laser output linewidth from few or few tenth of nm down to few pm or even single mode operation without a decrease in output power [12 , 13]. The properties of VBG have been described in Section 2.2.2.

In this thesis, a VBG is used as an output coupler and wavelength selector for obtaining single-frequency-mode generation in an Nd:$GdVO_4$ laser. Changing the temperature of the VBG can move the central peak and then to tune laser emission central wavelength.

2.3.3 Diode-Pumping of Solid State Laser

Diode pumped solid state (DPSS) lasers are solid state lasers made by pumping a solid gain medium with a laser diode. DPSS lasers are efficient because the diode laser provide direct excitation of the pump beam into the absorption band of the gain medium. And the diode laser itself has an efficient conversion of electric energy to optical energy. Although the beam quality of a laser diode is not good, it is possible to form a single TEM_{00} operation through the DPSS laser configuration. There are two types of pumping configuration: side-pumped and end-pumped configurations. In this thesis work, a diode-end-pump solid state laser was developed.

For optimal and efficient pumping, however, requirements have to be considered both spectrally and spatially. The spectral profile of the pump diode should be spectrally overlapped with the absorption line of the gain medium to obtain efficient absorption. And the beam profile of the pump diode should be spatially overlapped with the Gausisian mode of the laser cavity to obtain efficient excitation of only the

fundamental transverse cavity mode. A good spatial overlap can be obtained with focusing optics, though the diode laser usually has a divergent beam. The optimal way to do it is that the pump beam is focused to the Gaussian mode size. Besides, twice of Rayleigh length of the focused beam is not longer than the crystal length. Reshaping optics is required for diode lasers which have elliptical beams to obtain a circular spot before the pump beam reach the gain medium.

Chapter 3

Single Frequency 1070 nm Nd:$GdVO_4$ Laser Using a Volume Bragg Grating

3.1 Introduction

3.1.1 Motivation

Single frequency lasers are required in the spectroscopy of thallium atom for testing new physics beyond the standard model, which predicts atomic PNC effect arising from exchange of a Z_0-Boson between atomic electrons and nucleons. Atomic thallium (Z = 81) plays an important role in PNC experiments, since the PNC effect grows faster than Z^3. The PNC effect has been observed in atomic thallium system using $6P_{1/2} \rightarrow 6P_{3/2}$ transition in 1995 [3,4]. Laser cooling of thallium atoms, in which a 535 nm laser is needed, can improve the atomic PNC measurement. It is reasonable to obtain a 535 nm laser from a frequency doubled 1070 nm solid state laser.

3.1.2 Laser Material

DPSS lasers with advantages of good stability, narrow linewidth, and good beam quality have been found to be outstanding light sources for spectroscopy. Neodymium-doped gadolinium orthovanadate (Nd:$GdVO_4$) is an ideal laser crystal for the DPSS lasers due to its high pump absorption coefficient and large thermal conductivity [73, 74]. Most researches involving Nd:$GdVO_4$ crystal focused on the high power output at wavelength 1064 nm of the main gain peak [75], however, the fluorescence spectrum of a 0.5 at.% Nd:$GdVO_4$ crystal [71], reveals that there are some weaker emission bands around the main peak. One of the weak emission bands is located at 1070.8 nm which is only 6 nm away from the main peak. As a consequence, a 535 nm light source could be acquired by the second harmonic generation from a

1070 nm laser using Nd:$GdVO_4$ crystal. The properties of the Nd:$GdVO_4$ crystal has been described in Chapter 2.3.1

3.1.3 Laser Narrowing by Volume Bragg Grating

To achieve single frequency operation for DPSS, wavelength selection elements are required. From the fluorescence spectrum of a 0.5% at. Nd:$GdVO_4$ crystal (Fig. 1-2), the emission cross section at 1070.8 nm is about 20% of that at 1063.2 nm. Therefore, to obtain a 1070 nm laser operation with Nd:$GdVO_4$ crystal, one must suppress the laser action at 1063.2 nm. A 1083 nm Nd:$GdVO_4$ laser has been demonstrated using a specially coated dielectric mirror with high reflectivity at 1082.6 nm and lower reflectivity around 1060 nm to suppress the lasing at 1064 nm [10]. However, the 1070 nm band is too close to be separated from the 1064 nm band by a dielectric coated mirror. Other methods for wavelength selection were achieved by inserting an intra-cavity dispersive element, e.g. etalon, which introduces additional loss in the laser resonators resulting in raising the lasing threshold.

VBG offer an alternative approach for wavelength selection and line narrowing for solid state lasers [12]. VBG is a periodic phase grating recorded in PTR glass by thermal development after holographic exposure to UV radiation. PTR glass possesses large transparent range with low loss, high damage threshold, and good thermal stability. PTR VBG has extremely narrow spectral width (below 1 nm), good angular selectivity (below 10 mrad), and high relative diffractive efficiency (above 99.9%). These unique features make VBG ideal for working as intracavity wavelength selectors or resonator couplers in various types of lasers, depending on designed properties. VBG properties have been described in Section 2.2. CW single-longitudinal-mode Nd:$GdVO_4$ laser operation has been achieved with a short VBG Fabry-Perot cavity [40]

or a monolithic VBG cavity [43]. The monolithic VBG cavity provides over 80 GHz single frequency tuning range. However, the power is limited to 30 mW for single frequency operation by the high intracavity loss (~ 10%). In addition, it is not easy to perform fast frequency modulation which is often needed in laser spectroscopy. Figure 3-1 shows the center wavelength and bandwidth of our VBG and the fluorescence spectrum of the Nd:$GdVO_4$ laser crystal.

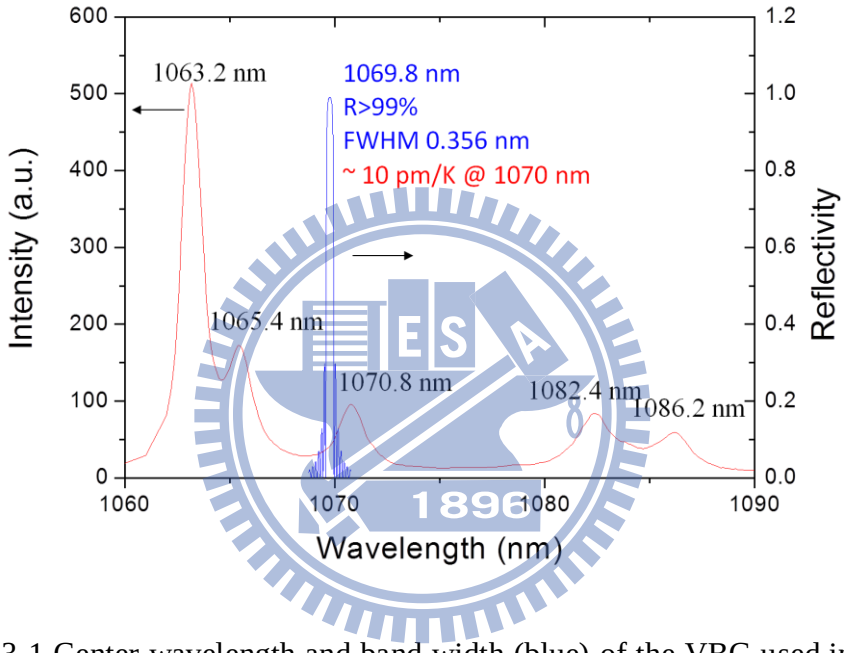

Fig. 3-1 Center wavelength and band width (blue) of the VBG used in this laser cavity and fluorescence spectrum (red) of the 0.5% at. Nd:$GdVO_4$ at room temperature

3.2 Experiments and Results

3.2.1 Experimental Setup of the Nd:$GdVO_4$ laser

The schematic diagram of the single frequency Nd:$GdVO_4$ laser is shown in Fig. 3-2. A short plano-concave cavity was employed in our work. An 808-nm fiber-coupled diode laser with a core-diameter of 800 μm and a numerical aperture of 0.12 served as

the pump source. The pump beam from the fiber end was focused into the laser crystal with a diameter of about 300 μm through the focusing optics formed by a pair of lenses. The cavity mirror M1 was a concave mirror with radius of curvature of 300 mm. It had anti-reflection (AR) coating at 808 nm (R < 0.5%) and 1064 nm (R < 0.2%) on the flat face, as well as AR coating at 808 nm (R < 5%) and high-reflection (HR) coating at 1064 nm (R > 99.8%) on the curved face. It was mounted on a PZT for fine tuning the laser cavity length. An a-cut 0.5% at. Nd:$GdVO_4$ crystal with a dimension of 3 × 3 × 4 mm^3 was used as the laser gain medium. The crystal was AR coated at 808 nm (R < 2%) and 1064 nm (R < 0.2%) on the side near M1 and AR (R < 0.2%) coated at 1064 nm and 532 nm on the other side. It was wrapped with an indium foil and mounted in a copper heat sink plate without temperature control and placed closely to M1. A PTR VBG (Optigrate Inc.) having peak reflectivity > 99% at center wavelength 1069.8 nm with FWHM of 0.356 nm and dimension of 5 × 5 × 4 mm^3 worked as the output coupler of the laser cavity. The VBG was AR coated at 1064 nm on both facets. It was wrapped with an indium foil and mounted in a copper heat sink and its temperature could be controlled at 15 to 60 ℃ by a thermoelectric cooler underneath. The distance between M1 and VBG was 10 mm. The output power was measured by a power meter (Scientech 362) at a distance of 100 mm from the VBG output coupler. The output spectrum was monitored by a home-made scanning confocal Fabry-Perot interferometer (FPI) with free spectral range of 1.5 GHz. An InGaAs detector (Thorlabs DET410) connected to an oscilloscope (Tektronix TDS 2024) was used to detect the spectrum signal after FPI. A wavemeter (Burleigh WA1000) and a beam analyzer (DataRay WinCamD) were used to verify the output wavelength and to monitor the output transverse beam profile respectively.

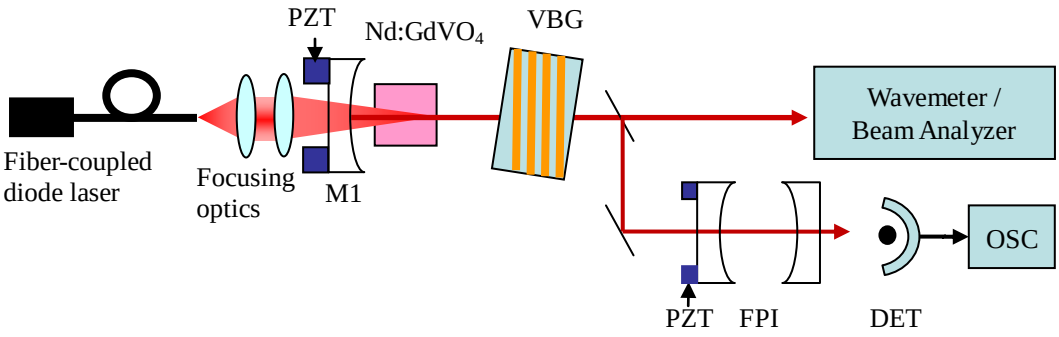

Fig. 3-2 Schematic diagram of the single frequency laser. Here, PZT: piezoelectric transducer; FPI: Fabry-Perot Interferometer; DET: detector; OSC: oscilloscope.

3.2.2 Output Properties of the Single Frequency Nd:$GdVO_4$ Laser

The single frequency operation of this plano-concave cavity laser was achieved by the VBG which acted as an output coupler and a wavelength selector. It should be mentioned that there were four weak beams surrounding the laser output beam. These beams were due to the grating plane in VBG was not parallel to the VBG surface and the reflection of VBG surfaces. They can be used to monitor the single frequency operation with the FPI. The output spectrum (shown in Fig. 3-3) monitored by the FPI indicates that the laser was operated at single frequency. The odd FPI trace was due to discrete sampling of digital oscilloscope. The detail output spectral profile (shown in the inset of Fig. 3-3) of the FPI at output power 200 mW showed a linewdith of 23 MHz which was limited by the instrument resolution of the FPI. The wavelength of the laser output could be tuned by the VBG temperature at a tuning coefficient of ~ 10 pm/K (or ~ −2.6 GHz/K). The vacuum wavelength of the laser was 1070.205 nm (280126.5 GHz) when the VBG was kept at 26 ℃. From the Fabry-Perot traces the

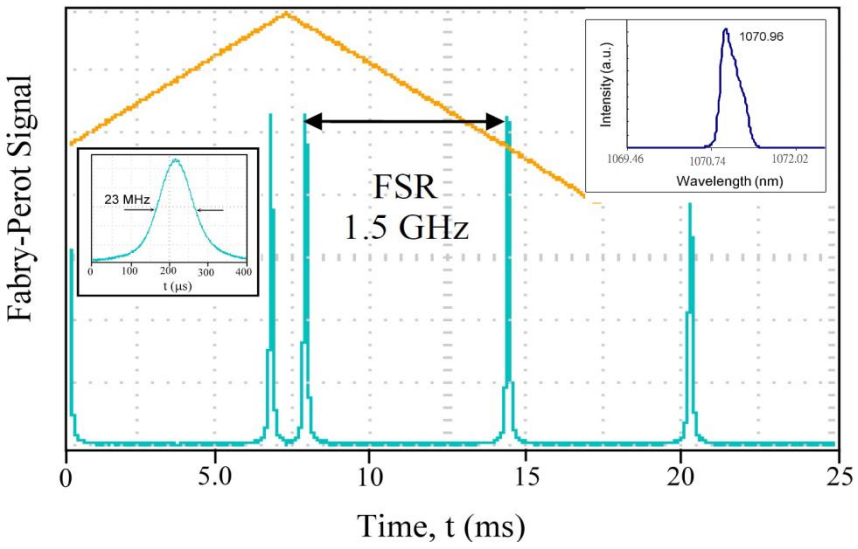

Fig. 3-3 Fabry-Perot trace of the single frequency Nd:GdVO4 laser. The inset shows details of the peak. Right inset shows 1070 nm laser spectrum by OSA

single frequency tuning range by the PZT tuning was about 5.1 GHz at output power 100 mW. The far-field spatial distribution of the beam at output power 200 mW measured by a beam analyzer is shown in Fig. 3-4. A nearly Gaussian intensity profile with good circularity was observed at a distance 45 cm from the output coupler. The

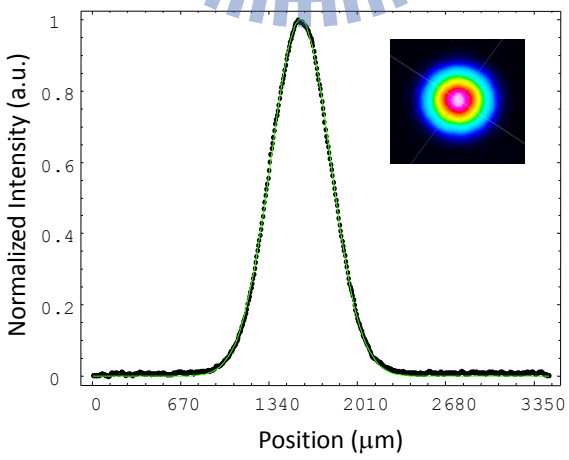

Fig. 3-4 The far-field intensity distribution of the 1070 nm laser at 200 mW output power. The solid curve is the fitted Gaussian distribution.

far field divergence angle of the laser output was around 0.37°. To check the beam quality of this laser, we measured the beam radius for the output beam at the 200 mW power level at different distances from a lens with focal length of 100 mm. The measured beam propagation parameter M^2 was 1.16.

However, the optimal position of focusing optics depends on the pump power as a result of thermal lens effect of the laser crystal under pumping. We need to fine-tune both the focusing optics position and the VBG angle to acquire a single mode laser with a maximum output power at different pump powers. Figure 3-5 shows the experimental results for the optimal output power for single frequency operation as a function of the pump power. Since the current of 808 nm pump laser could be adjusted by an increment of 1 Amp only, the slope efficiency of 14.5% and threshold pump power of 720 mW were obtained by a linear fitting. A single frequency laser output power of 300 mW had been obtained, limited by the reflectivity of the VBG, and it was difficult to obtain single frequency for higher output power. This fine-tuning procedure makes this laser inappropriate for applications where varying laser power is of prime importance.

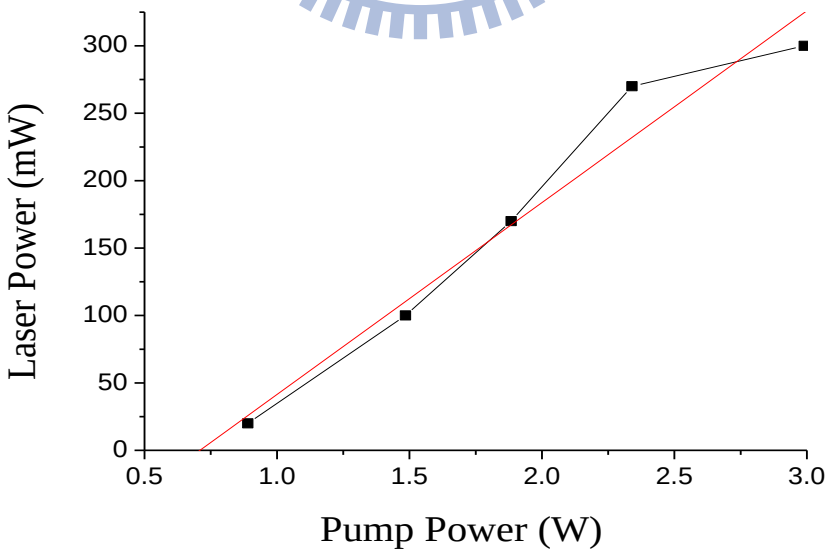

Fig. 3-5 1070 nm laser single frequency output power as a function of the incident pump power. The red line is the linear fitting result.

3.2.3 Frequency Stabilization

To demonstrate the application of this laser to spectroscopy, the resonance peak of the FPI cavity was used as a reference for locking the laser frequency. The experimental arrangement is shown in Fig. 3-6. A sinusoidal signal with a modulation frequency of 20 kHz was sent to the input channel 1 of a piezo amplifier (Physik Instrument E663). The PZT attached on one of the FPI cavity mirrors was driven by the output 1 of E663 to dither FPI cavity. To get a proper error signal for frequency locking, the transmitted light after the FPI was demodulated by a lock-in amplifier (Stanford Research SR844). The error signal from the lock-in amplifier was further sent to a PI (proportional and integral) servo controller (Precision Photonics LB1005). The output from LB1005 was amplified by the channel 2 of E663 to drive a piezoelectric actuator attached on the input mirror of the laser cavity for adjusting the cavity length to stabilize the laser frequency.

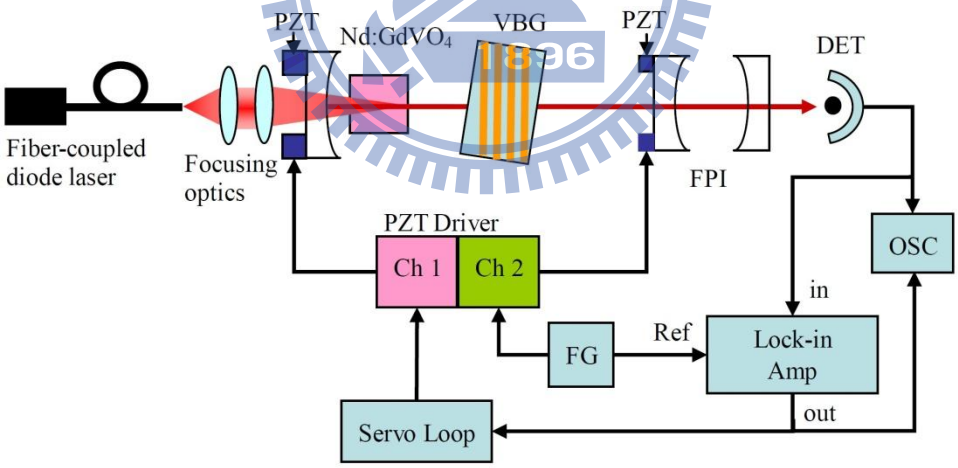

Fig. 3-6 Schematic diagram of the frequency stabilization setup. Here, VBG: volume Bragg grating; PZT: piezoelectric transducer; FPI: Fabry-Perot Interferometer; DET: detector; OSC: oscilloscope; FG: function generator

The first-derivative resonance signal obtained by the lock-in amplifier at 3 sec time constant while scanning the laser frequency is shown in Fig. 3-7(a). This first-derivative signal is proportional to the difference between the laser frequency and the cavity resonance near the resonance center and it was served as the error signal for frequency locking. The error signal was sent to a servo controller and amplified by a piezo controller to stabilize laser frequency. The slope of this frequency discriminator is 0.77 V/MHz. Figure 3-7(b) shows the error signal after the laser frequency was locked, which is proportional to the fluctuation of the laser frequency. From the error signal fluctuation we estimate that the peak-to-peak frequency fluctuation is 7.58 kHz (or 2.5 $\times 10^{-11}$).

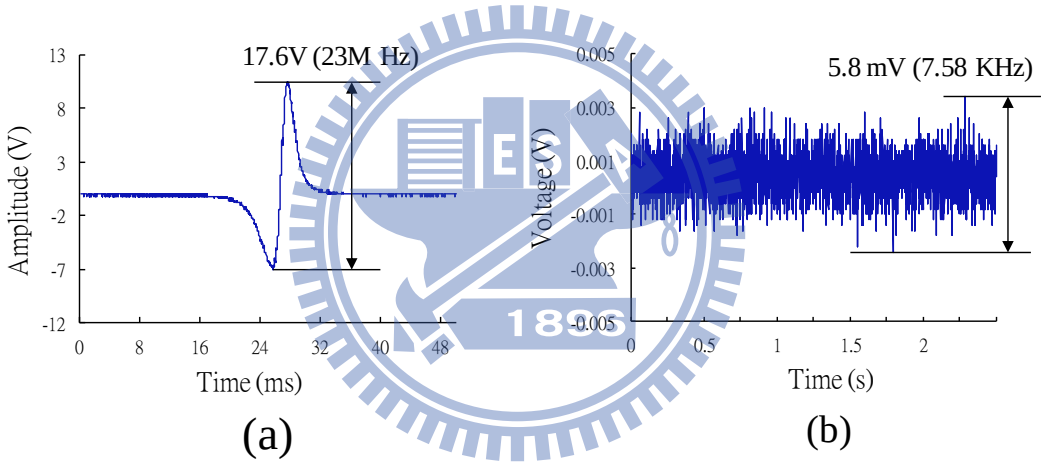

Fig. 3-7 (a) Error signal obtained by scanning laser frequency across the resonance peak. (b) Error signal after laser was locked.

3.3 Laser with Spherical-flat Laser Crystal

A new 1070 nm laser, which is similar to the early version except that that a Nd:$GdVO_4$ laser crystal with a spherical input surface (R= 30 cm, HT at 808 nm, HR at 1070 nm) and a flat end surface (AR at 808 nm and 1070 nm) is adopted to replace the concave cavity mirror and the flat-flat Nd:$GdVO_4$ laser crystal to increase the

frequency stability, is shown in Fig. 3-8. Figure 3-9 shows the 3D laser structure. The 1070-nm Nd:$GdVO_4$ laser also used a VBG as the output coupler and the wavelength selector. The spherical surface of this laser crystal acted as the concave mirror of the plano-concave laser cavity. The laser crystal was mounted on a PZT for cavity length tuning. To reduce the environmental disturbances, the entire laser assembly was put in an aluminum housing whose temperature was stabilized by a thermoelectric cooler. The frequency of the laser can be tuned coarsely by the VBG temperature and finely by the PZT voltage. The VBG is heated to ~45℃ and ~42.5℃ to generate the correct

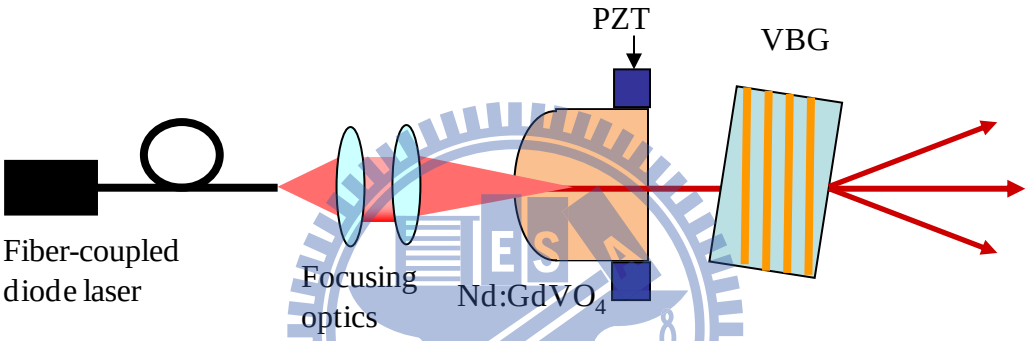

Fig. 3-8 Schematic diagram of the single frequency Nd:$GdVO_4$ laser

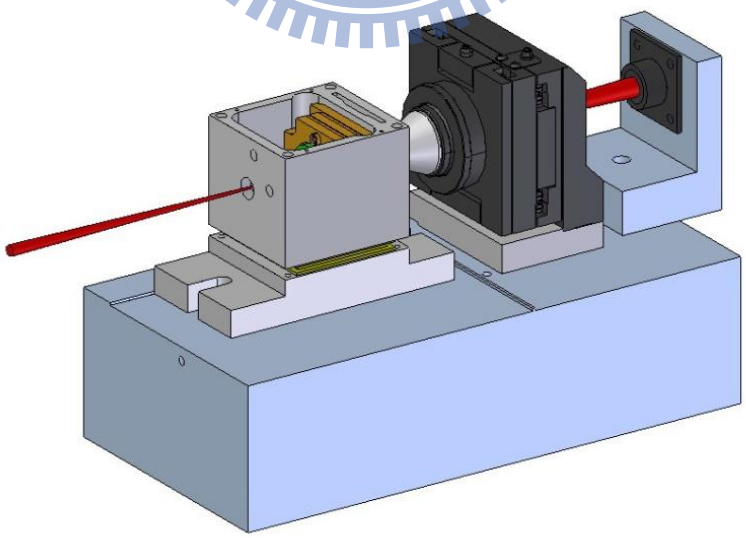

Fig. 3-9 3D laser structure

wavelength for iodine and thallium spectrum measurements, respectively. After fine tuning the VBG angle, we found that under this structure there were three main output beams due to the reflections of the Bragg grating planes and the VBG surfaces. All outputs were linearly polarized. The central beam of the three output laser beams was used to carry out our spectroscopy experiments.

3.4 Laser Frequency Stabilization

To reduce the laser frequency drift it was locked to a confocal Fabry-Perot interferometer (FPI). One of the side beams was directed into the confocal FPI and the FPI cavity length was modulated at 1.3 kHz. The 1070 nm light signal after the FPI cavity was demodulated to obtain the error signal for locking the laser frequency to the FPI. The laser frequency was then tuned by scanning the FPI cavity length after it was locked.

3.5 Second Harmonic Generation 535 nm Laser

The power of the central beam is boosted by a 900-mW Yb-doped fiber amplifier. The amplified 1070 nm laser beam was then focused into a 50 mm long MgO:PPLN crystal with a lens (f = 100 mm) for frequency doubling, shown in Fig. 3-10. The PPLN crystal was mounted in a temperature-stabilized oven and the quasi-phase matching condition was achieved around 107 ℃ and 101 ℃ for iodine and thallium spectrum measurement, respectively. After passing through the PPLN, the frequency doubled 535-nm light was collimated to 8.4 mm in diameter. The 1070 nm light was separated out by two dichroic mirrors (DMs). The 535 nm green light power after these two DMs was typically 46 mW at an input IR power of 700 mW to the PPLN, which corresponds to 6.5% power conversion efficiency.

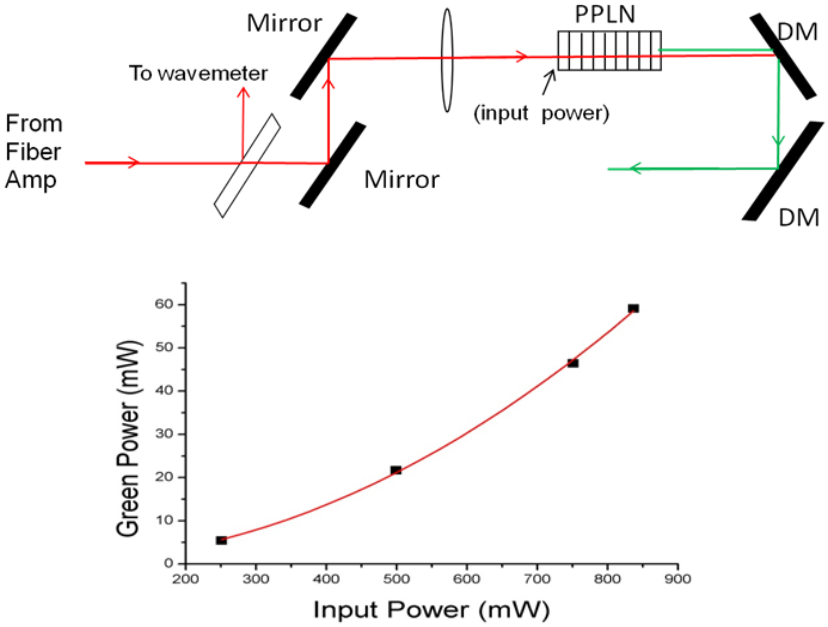

Fig. 3-10 Second harmonic generation of 535 nm laser

Chapter 4

Absolute Frequency Measurements of the Molecular Iodine Hyperfine Transitions at 535 nm

4.1 Introduction

The broad spectrum of molecular iodine has been widely used for optical wavelength reference or laser frequency stabilization in the visible and near infrared region. The iodine-stabilized lasers provide frequency references for various high precision atomic experiments [76-80] and several of them are recommended as the wavelength standards by the Comité International des Poids et Mesures [14, 15]. The extensive precision measurements of iodine spectrum allow us to characterize and calculate the iodine hyperfine structures [16]. The accuracy of the calculation depends on the high precision transition frequencies measured by available stable laser sources. DPSS lasers with good beam quality, narrow linewidth, and high stability are outstanding light sources for laser spectroscopy. Nonlinear optical-frequency conversion such as second harmonic generation enables the infrared DPSS laser to be locked to the hyperfine transitions of molecular iodine in the visible. For example, the iodine-stabilized frequency doubled Nd:YAG lasers at 532 nm show excellent stability and the absolute frequencies of iodine hyperfine transitions near 532 nm have been measured to very high accuracy using the optical frequency comb (OFC) [81-85].

In this work we present the Doppler-free saturation spectroscopy of the hyperfine transitions of $^{127}I_2$ P(28) 30-0 line at 535 nm using a frequency doubled 1070-nm Nd:$GdVO_4$ laser. Saturation spectroscopy was used to observe the hyperfine spectrum. The Nd:$GdVO_4$ laser was stabilized to the a_1, a_{10}, and a_{15} hyperfine components and their absolute frequencies were measured by an OFC. The pressure shift was investigated to obtain the absolute frequency at zero pressure. The effect of

pressure and power broadening of the a_{10} component were also investigated. Our results are useful for improving the theoretical calculation. In addition, the frequency of this iodine line is very close to the $6P_{3/2} \rightarrow 7S_{1/2}$ transition of the thallium atom. Therefore, this laser was proved to be useful for measuring the $6P_{3/2} \rightarrow 7S_{1/2}$ transition frequency in thallium.

4.2 Experimental Setup

4.2.1 Laser Setup for Iodine Spectrum

The schematic diagram of our experiment is shown in Fig. 4-1. The laser source was a frequency doubled 1070-nm Nd:$GdVO_4$ laser, which have been described in Chapter

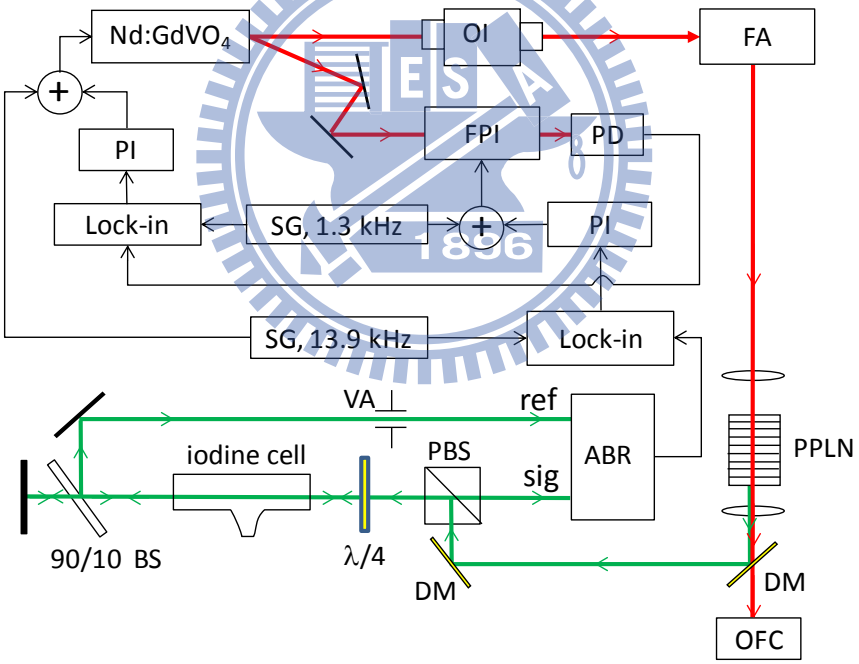

Fig. 4-1 Experimental layout of the iodine laser stabilization. OI: optical isolator, FA: fiber amplifier, FPI: Fabry-Perot interferometer, PD: photodiode, PI: PI servo loop, SG: signal generator, Lock-in: Lock-in amplifier, VA: variable aperture, ABR: auto-balanced receiver, BS: beam splitter, λ/4: quarter-wave plate, DM, dichroic mirror.

3.3. The frequency of the laser can be tuned coarsely by the VBG temperature and finely by the PZT voltage. The VBG temperature was set to 45℃ for the iodine P(28) 30-0 line wavelength. The laser frequency was locked to the FPI to reduce its frequency jitter. To lock the laser to the FPI, the FPI cavity length was modulated at 1.3 kHz. The amplified 1070 nm light by a 900-mW Yb-doped fiber amplifier went through the PPLN to generate a 535 nm light by second harmonic generation. The PPLN crystal mounted in a temperature-stabilized oven was around 107 ℃ to achieve the quasi-phase matching condition for iodine P(28) 30-0 line and thallium. After passing through the PPLN, the frequency doubled 535-nm light was collimated to 8.4 mm in diameter. The 1070 nm light was separated out by two DMs. The 1070 nm light passing through the first DM was transferred to an OFC [17] by a polarization maintaining single-mode fiber for frequency measurement.

4.2.2 Iodine Absorption Spectroscopy Experiment

The SHG 535 nm light was used to observed the saturation absorption signal of the hyperfine components of the P(28) 30-0 line in an iodine vapor cell. The linear polarized green light passing through a polarizing beam splitter (PBS) and a quarter-wave plate (λ/4) was transformed into circularly polarized light, and goes through an iodine vapor cell acting as the saturating beam. The 6 cm long iodine vapor cell with plane windows was slightly tilted in the beam direction to prevent back-reflection into the laser system. The cold finger of the cell can be temperature controlled from 0 to 23 ℃ and accordingly the iodine vapor pressure from 4.1 to 34.9 Pa. The circular polarized green light was further separated by a 90/10 beam splitter (BS). The weaker beam after the BS was retro-reflected by a mirror into the iodine cell controlled from 0 to 23 ℃ and accordingly the iodine vapor pressure from 4.1 to 34.9

Pa. The circular polarized green light was further separated by a 90/10 beam splitter (BS). The weaker beam after the BS was retro-reflected by a mirror into the iodine cell acting as the probe beam. Then it passes through the λ/4 plate and PBS to the signal input of an auto-balanced receiver (New Focus 2017 Nirvana). The stronger beam was directed into the reference input of the auto-balanced receiver. The auto-balanced receiver was used to suppress the intensity noise of the 535-nm light. The optimum ratio of signal and reference optical powers for noise cancellation was achieved by a variable aperture in front of the reference input. The signal monitor port of the receiver was used to observe the probe beam intensity. To obtain the third-derivative saturated absorption signal of the iodine P(28) 30-0 line for frequency locking the laser frequency was modulated at 13.9 kHz. The balanced signal from the receiver was demodulated with a lock-in amplifier (Standard Research Systems SR830) at the third-harmonic of 13.9 kHz. The time constant was set to 30 ms at 12 dB/oct. To lock the laser frequency to the hyperfine transition, the resulting third derivative signal was feed through a PI (proportional and integral) servo loop to control the FPI cavity length.

4.2.3 Iodine Absolute Frequency Measurement

Once the laser was locked to one of the hyperfine transitions, the 1070 nm laser frequency was measured by a self-referenced OFC [17], which was based on a 1-GHz mode-locked Ti:sapphire laser with spectrum expanded using a microstructure fiber. The repetition frequency f_{rep} and offset frequency f_{offset} of our OFC are phase locked to a GPS-disciplined Rb clock. The accuracy of our OFC is better than 1×10^{-12} at a 1000-sec measurement time. The transition frequency is determined by the following relation:

$$f_{iodine} = 2 f_{IR} = 2(N f_{rep} \pm f_{offset} \pm f_{beat}), \tag{4.1}$$

where N is a mode number and f_{beat} is the beat frequency between laser and the nearest comb line. To determine N, the laser frequency was measured by a wavemeter with uncertainty less than 1 GHz. The absorption spectrum was also scanned over a range of several GHz to identify the transitions according the pattern predicted by the IodineSpec5 [16]. The repetition rate was much larger than the expected uncertainty of IodineSpec5, so the mode number N can be determined by comparing the resulting frequency value using Eq. 4.1 with the IodineSpec5 prediction. The frequency measurement was further confirmed using different repetition rate and offset frequency of the OFC.

4.3 Results and Discussions

4.3.1 Iodine Absorption Spectrum

Figure 4-2 shows the saturation absorption spectrum of the P(28) 30-0 line of $^{127}I_2$ at 535 nm using the third-harmonic demodulation method. Here, the 1070 nm laser was locked to the FPI cavity and the laser frequency was scanned across the molecular iodine resonance by tuning the FPI cavity length. The 535 nm optical powers of the pump and probe beams, both having a diameter of 8.4 mm, were 22.9 mW and 0.39 mW, respectively. The optical intensity of the probe beam was slightly different for each hyperfine transition due to the iodine absorption. The cold-finger temperature of the iodine cell was held at 14.5 ℃ to keep the pressure at 16.5 Pa inside the cell. The laser frequency was modulated at 13.9 kHz with a modulation width of 5.2 MHz for locking the laser frequency to the hyperfine transition. The well isolated a_1, a_{10}, and a_{15} hyperfine transitions were chosen for laser stabilization. The inset in Fig. 4-2 shows the third-derivative signal of the a_1 line. The signal-to-noise ratios of the a_1, a_{10} and a_{15} components at lock-in time constant 30 ms at 12dB/oct were approximately

1000, 500 and 900 respectively.

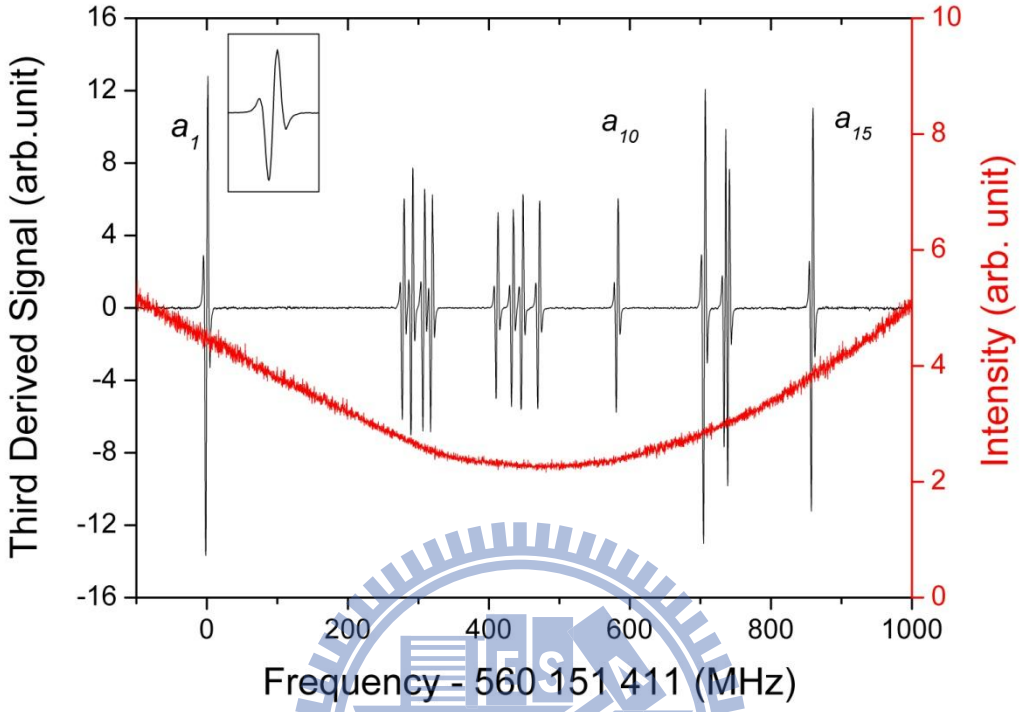

Fig. 4-2 Hyperfine spectrum a_1–a_{15} of the iodine P(28) 30-0 line and the probe beam intensity which represents the absorption profile. Inset is the signal of a1 component which shows a signal-to-noise ratio of 1000. Here, cold-finger temperature was 14.5 ℃ and the lock-in time constant was 30 ms at 12 dB/oct.

4.3.2 Frequency Stability of the Iodine Locked Laser

To investigate the laser frequency stability, the beat frequency was utilized to calculate the Allan deviation with 1000 data points, shown in Fig 4-3. The laser frequency had a fractional Allan deviation of 3×10^{-12} at 10 second averaging time, when the laser was stabilized to the a_1 component at iodine vapor pressure of 16.5 Pa.

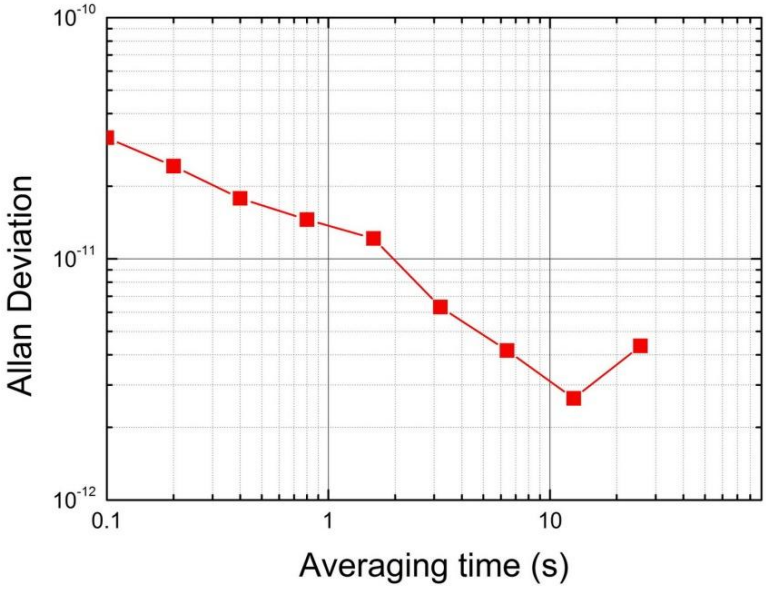

Fig. 4-3 Fractional Allan deviation of the measured beat frequency between the laser locked on a_1 component and the OFC.

4.3.3 Absolute Frequency Measurement of the Iodine Hyperfine Transition

The beat frequency between the iodine-stabilized 1070 nm laser and the OFC was measured using a high-frequency counter (Agilent A53150) with a 100 ms gate time and 500 data points were recorded for each beat frequency measurement. Then the average value was used to derive the absolute frequency of the hyperfine transition using Eq. 4.1.

To determine the transition frequency at zero pressure, the pressure shift must be investigated. For pressure shift measurement, the pump and probe powers were fixed at 22.9 mW and 0.39 mW respectively, and the cold finger temperature was changed to control the vapor pressure of the iodine cell. The iodine partial pressure inside the cell can be calculated according to the following formula [86],

$$\log(P) = \frac{-3512.830}{T} - 2.013 \cdot \log(T) + 18.37971, \qquad (4.2)$$

where P is the iodine vapor pressure in Pascal and T is the cold finger temperature in Kelvin. The cold finger temperature of the iodine cell was varied from 0.1 ℃ (4.2 Pa) to 20.2 ℃ (26.9 Pa). All the measured frequencies in the test pressure range were used to determine the zero-pressure absolute frequency and the pressure shift coefficient. Figure 4-4 shows the frequency measurement versus iodine vapor pressure. The statistical expected zero-pressure absolute frequencies were 560 151 411 260(2) kHz, 560 151 982 649(1) kHz and 560 152 269 813(1) kHz for the a_1, a_{10}, and a_{15} components respectively. The pressure shift coefficients for the a_1, a_{10}, and a_{15} components deduced from the linear relationship of the measured absolute frequencies versus vapor pressures were -5.28 ± 0.08 kHz/Pa, -5.23 ± 0.07 kHz/Pa and -5.12 ± 0.05 kHz/Pa for the a_1, a_{10}, and a_{15} components.

Besides the correction of the pressure shift, another systematic uncertainty come from the servo-loop electronics was found to be around 10 kHz. The DC offset from the lock-in amplifier also enters into an uncertainty of around 2 kHz. Table 4-1 shows the measurement results of the three transition frequencies during one month and the comparisons with the calculated values.

Table 4-1 Selected hyperfine transition frequencies of the P(28) 30-0 line and comparisons to the calculated values (kHz)

	Measured[a]	Calculated[b]	Measured– Calculated
a_1	560 151 411 260 (11)	560 151 405 525	5735
a_{10}	560 151 982 649 (11)	560 151 976 906	5743
a_{15}	560 152 269 813 (11)	560 152 264 072	5741

[a]the uncertainty is the combined error of statistical error and another systematic uncertainties which come from the servo loop and the DC offset of the lock-in amplifier.
[b]Calculated from IodineSpec5 [16]

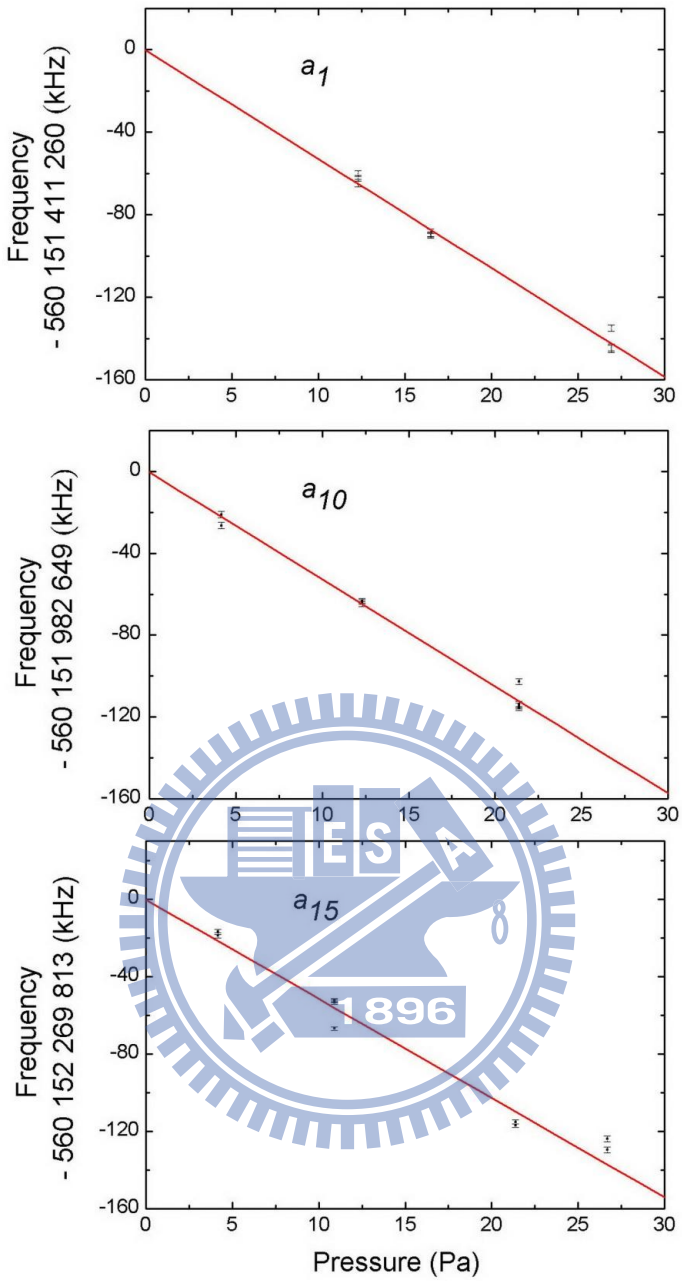

Fig. 4-4 Measured absolute frequencies versus iodine vapor pressures for hyperfine components a_1, a_{10}, and a_{15}. Each data point represents the mean value of 500 measurements. The standard deviation of the 500 measurements divided by the square root of 500 was assigned as the error bar of each data point.

4.3.4 Pressure and Power Broadening of the Iodine Hyperfine Component

To investigate the pressure and power broadening of the a_{10} component, we adopt the method proposed by Fang *et al.* [87] to determine the linewidth by measuring the dependence of the peak amplitude of the third-derivative signal on the modulation width. The peak amplitude of the third-derivative signal on the normalized modulation width δ_A can be written as

$$h(\delta_A) = C \cdot (P_1\delta_A + P_2\delta_A^2 + P_3\delta_A^3) / (P_4 + P_5\delta_A + P_6\delta_A^2 + P_7\delta_A^3), \qquad (4.3)$$

where $\delta_A = d_A / d_h$, d_A is the modulation amplitude, d_h is the half-width at half-maximum of the transition line, and C is a constant. The coefficients are P_1 = -1.51636, P_2 = 6.89591, P_3 = -0.09229, P_4 = 48.96763, P_5 = -3.70996, P_6 = 16.56378, and P_7 = 1.93711. For the pressure broadening measurement, the pump and probe powers were fixed at 22.9 mW and 0.39 mW, and the cold finger temperature of the iodine cell was varied from 0.1 ℃ (4.2 Pa) to 20.2 ℃ (26.9 Pa). Figure 4-5 shows the variation of the linewidth with iodine vapor pressure. The inset in Fig. 4-5 shows the measured peak amplitude of the third-derivative signal versus the modulation amplitude of the a_{10} component under different vapor pressure. The pressure broadening coefficient was 125(14) kHz/Pa and the zero-pressure linewidth was 3.72(19) MHz. For the power broadening experiment, shown in Fig. 4-6, the cold finger temperature of the iodine cell was fixed at 0.1 ℃ (4.2 Pa), and the pump power was changed from 4.6 to 41.3 mW. The probe power was fixed at 1.7% of the pump power. The inset in Fig. 4-6 shows the measured peak amplitude of the third-derivative signal versus the modulation amplitude of the a_{10} component under different pump power. The relation of linewidth and the pump power is [88],

$$\gamma' = \gamma(1 + \sqrt{1 + P / P_s}), \qquad (4.4)$$

where γ is the linewidth associated with the limit of weak saturating and probe beams,

P is the power in the saturating beam and P_S is the saturation power. Through a nonlinear least-squares fit to the data in Fig. 4-6, we obtained γ = 1.91(4) MHz and P_S = 28.6 mW, corresponding to a saturation intensity of 51.6 mW/cm^2. However, the saturation intensity was not reliable due to the limited available data points. With a linear fit the measured power broadening slope was 12.6(2) kHz/mW.

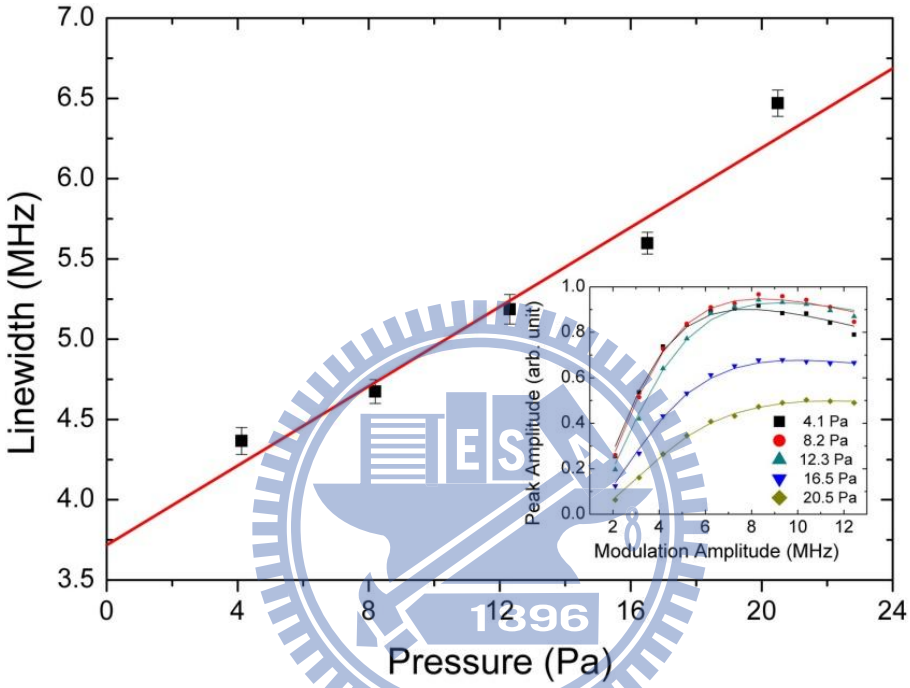

Fig. 4-5 Linewidth of a_{10} versus the iodine vapor pressure. The pump and probe powers were fixed at 22.9 mW and 0.39 mW. The inset shows the measured peak amplitude of the third-derivative signal versus the modulation amplitude under different vapor pressure. The solid curves in inset depict results of curve fitting.

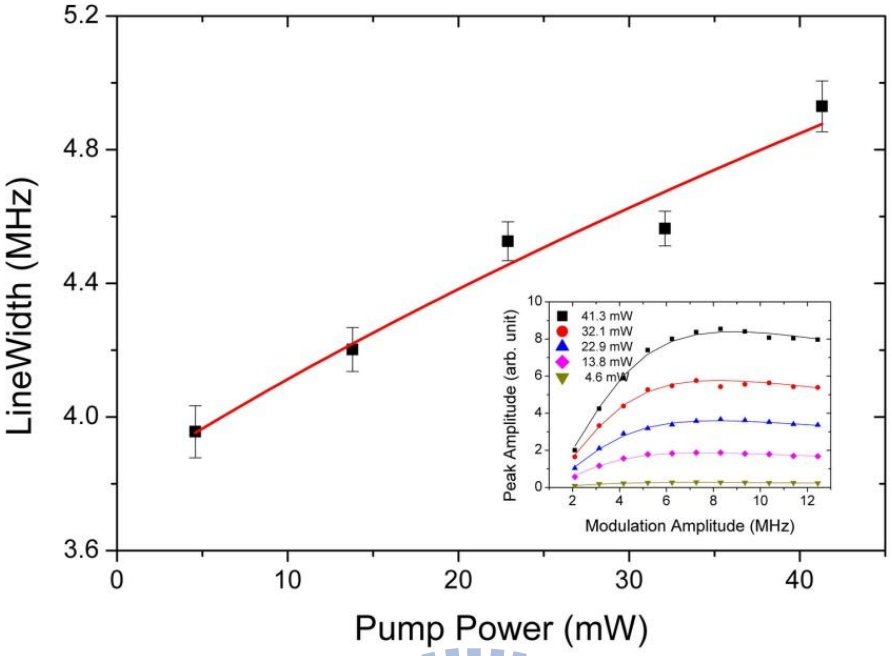

Fig. 4-6 Linewidth of a_{10} versus pump power. The cold finger temperature of the iodine cell was fixed at 0.1 ℃ (4.2 Pa). The inset shows the measured peak amplitude of the third-derivative signal on the modulation amplitude under different pump power. The solid curves in inset depict results of curve fitting.

Chapter 5

Frequency Measurement of the $6P_{3/2} \rightarrow 7S_{1/2}$ Transition of Thallium

5.1 Introduction

High precision measurement in atomic system shows very promising in testing new physics beyond the standard model which predicts atomic PNC effects arising from exchange of a Z_0 boson between atomic electrons and nucleons. Atomic PNC effects depend intimately on the behavior of the electron wave function near the nucleus. In the atomic PNC measurement an accurate theoretical calculation of atomic structure is needed for such test.

Atomic thallium (Z=81) plays an important role in PNC experiments, since PNC effect grows faster than Z^3. The PNC effect had been observed in atomic thallium system using $6P_{1/2} \rightarrow 6P_{3/2}$ transition in 1995 [3, 4]. The optical rotation measurement of thallium reached 1% of experimental uncertainty. Combining the theoretical calculation, it leads to the weak charge of thallium nucleus, which can be compared with the predication of the standard model. However, the dominating uncertainty is the theoretical calculation, which was as large as 3%. The hyperfine structure is sensitive to the wave functions at small distance from the nucleus. The measured absolute transition energy, HFS and IS of the thallium can provide important information concerning the nuclei to cross-check the theory calculation.

The simplified low-lying energy levels of thallium are shown in Fig. 5-1 with the most precise values of HFS and ISs. HFS measurements with uncertainties <1 kHz for both $6P_{1/2}$ and $6P_{3/2}$ states have been reported precise HFS using microwave magnetic resonance techniques in the 1950s [32, 33]. The absolute transition frequency and the HFS of the $6P_{1/2} \rightarrow 7S_{1/2}$ transition have also been reported [9]. However, no precise

measurements had been carried out for the $6P_{3/2} \rightarrow 7S_{1/2}$ transition at 535 nm.

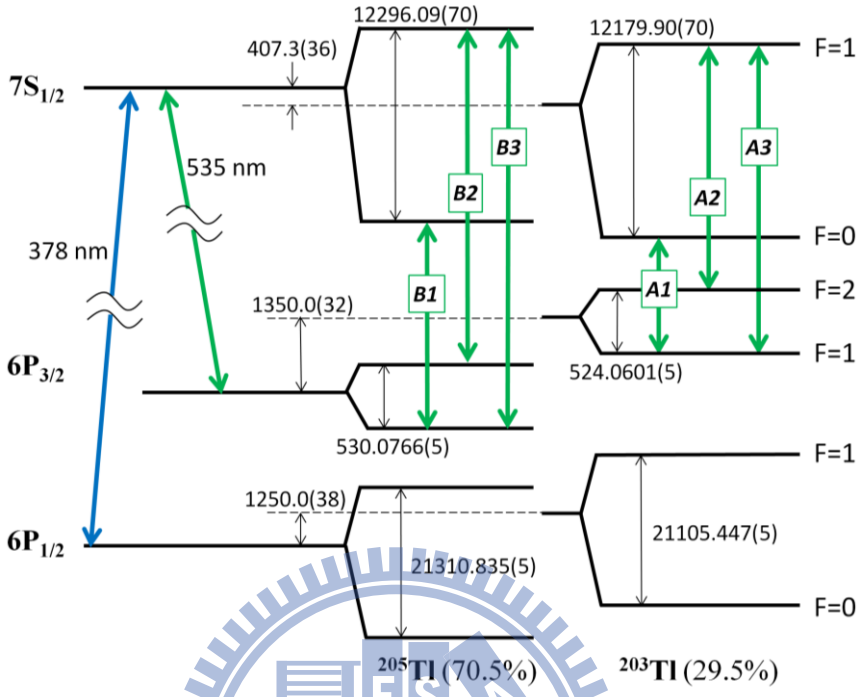

Fig. 5-1 Energy-level diagram of ^{203}Tl and ^{205}Tl with the hyperfine splittings and isotope level shifts in the unit of MHz. Energy levels are not to scale. The six lines investigated in this work are labeled A1, A2, A3 and B1, B2, B3. The hyperfine splittings of $6P_{1/2}$ and $6P_{3/2}$ are taken from [33] and [34], respectively. The hyperfine splittings of $7S_{1/2}$ are taken from [9]. The level ISs are taken from [35].

In this work, a precise measurement of the absolute frequencies of hyperfine components of the 535 nm $6P_{3/2} \rightarrow 7S_{1/2}$ transition for both Tl isotopes was achieved using the single frequency Nd:$GdVO_4$ laser. The results will serve as an experimental constrain for the improvement of theory calculation. A HCL was utilized to provide vapor of the atomic thallium at the metastable $6P_{3/2}$ state. The saturation spectroscopy was employed to resolve all the hyperfine transitions, and their absolute frequencies were measured using a precision wavelength meter.

5.2 Experimental Setup

5.2.1 Description to Laser Setup for Thallium Spectrum

The schematic of our experimental setup for the absolute frequency measurement of the hyperfine components in the 535 nm $6P_{3/2} \rightarrow 7S_{1/2}$ transition of Tl is shown in Fig. 5-2. The laser source is the frequency-doubled 1070-nm Nd:$GdVO_4$ laser. The laser used a VBG as the output coupler and the wavelength selector. The frequency of the laser can be tuned coarsely by the VBG temperature via thermal controlling the housing and finely by the PZT voltage. In our experiment, the VBG was heated to ~ 42.5 ℃ to generate the correct wavelength for the $6P_{3/2} \rightarrow 7S_{1/2}$ transition after frequency

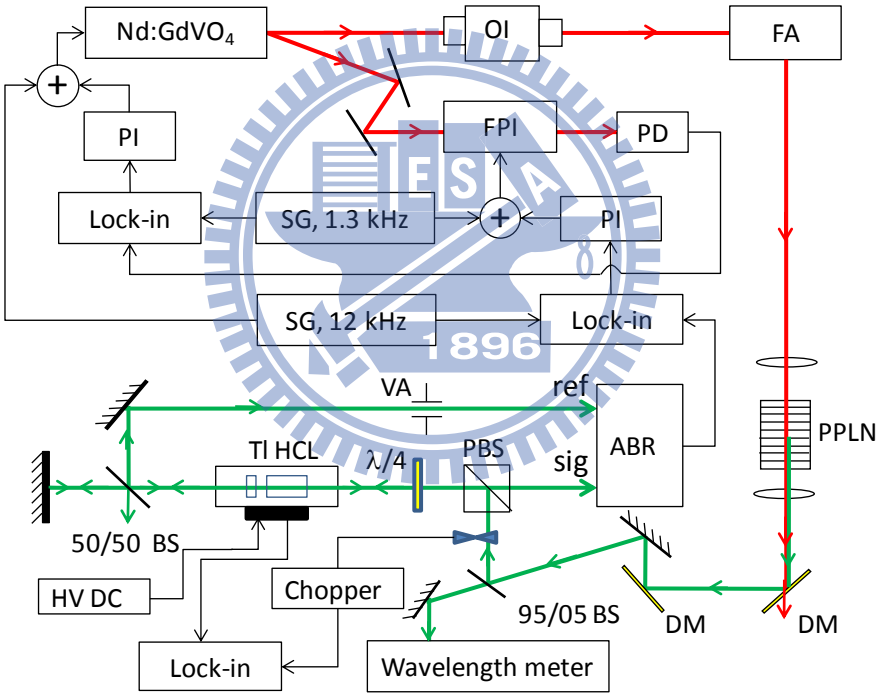

Fig. 5-2 Schematic of the experimental setup. OI: optical isolator, FA: fiber amplifier, FPI: Fabry-Perot interferometer, PD: photodiode, PI: PI servo loop, SG: signal generator, Lock-in: Lock-in amplifier, VA: variable aperture, ABR: auto-balanced receiver, BS: beam splitter, λ/4: quarter-wave plate, DM, dichroic mirror, HV DC: high voltage DC power supply for HCL.

doubling. By tuning the PZT, the single frequency tuning range without mode-hopping at total output power > 100 mW was about 5 GHz at 1070 nm, which was not wide enough to cover the whole $6P_{3/2} \rightarrow 7S_{1/2}$ hyperfine transition lines after frequency doubling. Therefore, the whole spectrum of $6P_{3/2} \rightarrow 7S_{1/2}$ transition was divided into two regions to be separately investigated and the center of each region was set by tuning the VBG temperature. To reduce the laser frequency drift it was locked to a confocal Fabry-Perot interferometer (FPI). The laser frequency was then tuned by scanning the FPI cavity length after it was locked.

The central beam of the VBG laser boosted by a 900-mW Yb-doped fiber was then focused into a 50 mm long MgO:PPLN crystal with a lens (f = 100 mm) for generating 535 nm Laser. The PPLN crystal was temperature-stabilized around 101 ℃ to achieve the quasi-phase matching condition for thallium $6P_{3/2} \rightarrow 7S_{1/2}$ transition. After passing through the PPLN, the 1070 nm light beam was separated out by two DMs and the second harmonic 535-nm green light was collimated to a beam size of 8.4 mm in diameter. The power of 535 nm light beams after these two DMs was typically 46 mW at 700mW 1070nm fundamental pump power.

5.2.2 See-Through Hollow Cathode Lamp and Optogalvanic Signal

A commercially available see-through HCL was used as the thallium atomic source. HCL is a metal-vapor discharge lamp specifically developed for atomic absorption spectroscopy and narrow band atomic line filter [89]. Exciting the HCL with a high voltage source, a discharge plasma is generated inside the cathode. HCL produces not only sufficient metal vapor without high temperature oven, but also the atoms at the excited states. When a laser enters the cathode and the atoms inside the discharge plasma resonantly interact with the incident photons, the electrical impedance of the

discharge plasma is altered, by which an optogalvanic (OG) signal is obtained. Optogalvanic effect has been widely used to stabilize laser frequency [90]. In our experiment, a Hamamatsu L2783-81 NE-TL see-through HCL was used as the thallium vapor cell. The cylindrical cathode (19 mm in length and 3 mm in diameter) and the ring anode are sealed with neon buffer gas at a pressure of 14 torr. The HCL was operated at a current of 10.7 mA with a 30 kΩ ballast resistor.

The absorption lines of thallium in the HCL are Doppler broadened by the random thermal motion of the thallium atoms. Saturated absorption spectroscopy was used to eliminate the Doppler-broadening by counter-propagating a strong pump beam over the probe beam. The linear polarized green light passes through a 95:5 (R:T) beam splitter (BS) reaches a precision wavelength meter (HighFinesse, WSU 30) for frequency measurement. The beam reflected by the BS was further reflected by a polarizing beam splitter (PBS) and transformed into circular polarization by a quarter-wave plate ($\lambda/4$), and then goes through the HCL acting as the pump beam. The circularly polarized green light was further separated by a 50/50 beam splitter. The beam passing through the BS was retro-reflected by a mirror into the HCL acting as the probe beam. The reflected light was then transformed into linear polarization by going through the $\lambda/4$ plate again and passes through the PBS to the signal input of an auto-balanced receiver (ABR, New Focus, 2017 Nirvana). The auto-balanced receiver was used to suppress the intensity noise of the 535 nm light. The counter-propagated pump and probe beams were overlapped within the HCL with powers of 12.5 mW and 2.7 mW, respectively. The beam reflected by the 50/50 BS was directed into the reference input of the auto-balanced receiver. The optimal power ratio of the signal to the reference beam for noise cancellation was achieved by a variable aperture in front of the reference input.

5.2.3 Thallium Absorption Spectrum

To tune the laser wavelength to the thallium transition, the 535 nm green light was first amplitude modulated by a mechanical chopper at 2 kHz. The optogalvanic signal from the HCL was detected with a lock-in amplifier (Standard Research Systems SR830) to obtain the Doppler broadened spectrum of the $6P_{3/2} \rightarrow 7S_{1/2}$ transition by tuning the laser frequency via scanning the FPI cavity length. To obtain the third-derivative saturated absorption spectrum of the hyperfine transition, the laser cavity length was modulated at 12 kHz and the balanced signal from the auto-balanced receiver was demodulated with a lock-in amplifier at the third harmonics (36 kHz). The time constant was set to 30ms at 12dB/oct. To lock the laser frequency to the center of the hyperfine transition, the demodulated signal was feed through a PI (proportional and integral) servo loop to control the FPI cavity length.

5.2.4 Wavelength Meter Calibration

The absolute transition frequencies were measured using the precision wavelength meter. It is a Fizeau based wavelength meter and a similar wavelength meter has been used to measure the hyperfine splitting in Cs to an accuracy of 0.5 MHz [91, 92]. Our wavelength meter has an absolute accuracy of 30 MHz in 10 h [18] after it is calibrated against a stabilized laser with an accurately known frequency. In our work, a frequency doubled Nd:YAG laser at 532 nm stabilized to the hyperfine component *a10* of *R*(56) 32-0 transition of molecular iodine was utilized to calibrate the wavelength meter. Its absolute frequency has been recommended as an optical frequency standard [14, 15]. We find that the drift of the wavelength meter was less than 1 MHz within 10 min after calibration. To check the accuracy of the wavelength meter at 535 nm, the frequency doubled Nd:$GdVO_4$ laser was stabilized to the hyperfine components of the *P*(28) 30-0

transition of molecular iodine at 535 nm, which is less than 10 GHz away from the thallium transitions. The absolute frequencies of the *a1*, *a10*, and *a15* hyperfine components have been measured using an optical frequency comb (OFC) to an accuracy of 11 kHz, described in Chapter 4. The differences between the absolute frequencies measured by the wavelength meter and the OFC were less than 3 MHz for all three hyperfine components. In addition, the separation of hyperfine components obtained by the wavelength meter was less than 1 MHz deviation from the values obtained by OFC. To avoid the long time drift in the wavelength meter during frequency measurement, the calibration using iodine-stabilized 532 nm laser was carried out every 10 min to assure the accuracy of our measurements was better than 30 MHz.

5.3 Experimental Results and Discussion

5.3.1 Thallium Hyperfine $6P_{3/2} \rightarrow 7S_{1/2}$ Transition Spectrum

The $6P_{3/2} \rightarrow 7S_{1/2}$ transition for ^{203}Tl and ^{205}Tl consists of six hyperfine components as shown in Fig. 5-1. These hyperfine components are labeled as A1, A2, A3 and B1, B2, B3 for ^{203}Tl and ^{205}Tl, respectively. The output of the lock-in detection of the discharge current modulation, due to the laser intensity modulation by the mechanical chopper, provides the OG spectrum shown in the upper curve of Fig. 5-3. The hyperfine components of $6_{P3/2} \rightarrow 7S_{1/2}$ transition are not resolved in the OG spectrum due to the Doppler broadening. The Doppler-free saturated absorption spectrum is shown in the lower part of Fig. 5-3. For the strongest component B2, the signal-to-noise ratio (SNR) was 220. The ratio of the signal strength between the observed transitions does not agree with the predicted strength based on the transition rate calculation (shown in the OG spectrum in Fig. 5-3). This discrepancy, which was also observed in the emission

profile of the earlier literature [89], was attributed to the high drive current of the HCL. The SNR of the A1, A2, B1, and B2 components was high enough for laser frequency stabilization and direct frequency measurement using the HighFinesse wavelength meter.

5.3.2 Spectral Linewith of the Thallium Hyperfine Transition

The observed saturated absorption spectrum shown in Fig. 5-3 was acquired using a frequency modulation width that was optimized for the third-derivative signal of the B2 component. For a spectral line with a Lorentzian profile, the third derivative signal

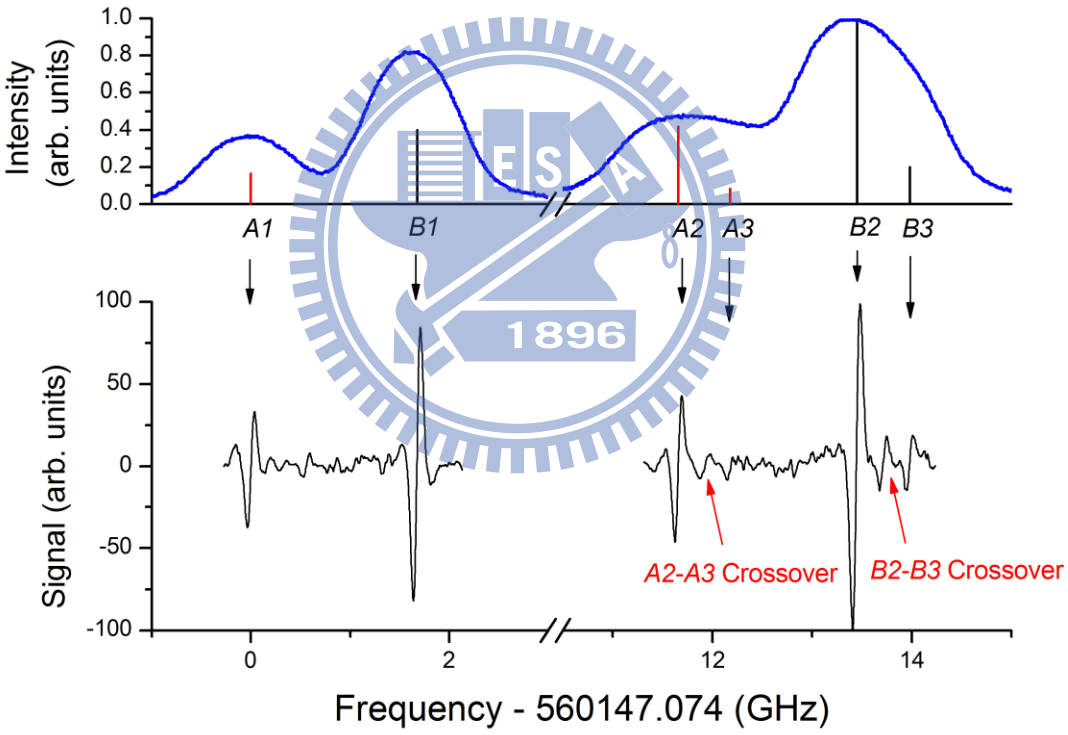

Fig. 5-3 Observed spectrum of hyperfine components of the $6P_{3/2} \rightarrow 7S_{1/2}$ transition in atomic thallium at 535 nm. The upper figure is the optogalvanic (OG) spectrum. Vertical lines show the calculated spectral intensity. The lower figure is the third-derivative signal of the saturated absorption spectrum.

reaches a maximum while the modulation width is 1.75 × FWHM (full width at half-maximum) and the peak-to-peak frequency interval then equals to 1.65 × FWHM [93]. The peak-to-peak frequency interval was 70 MHz in our experiment, thus the FWHM of the B2 component was 42 MHz. For comparison, the natural linewidth of the B2 component was estimated to be 17 MHz by the lifetime of $7S_{1/2}$ state [94].

5.3.3 Frequency Stability of the Frequency Locked Laser

The laser was locked to the zero-crossing points of the third derivative signal. The error signal of the stabilized laser was used to evaluate the stability of the laser frequency. The 70 MHz peak-to-peak frequency interval of the third-derivative signal of the B2 component was employed to determine the frequency discrimination slope. Figure 5-4 shows the Allan deviation for the frequency doubled Nd:$GdVO_4$ laser stabilized at the B2 component. The frequency stability was 30 kHz at 1 s averaging time and reaches 2 kHz at 10 s.

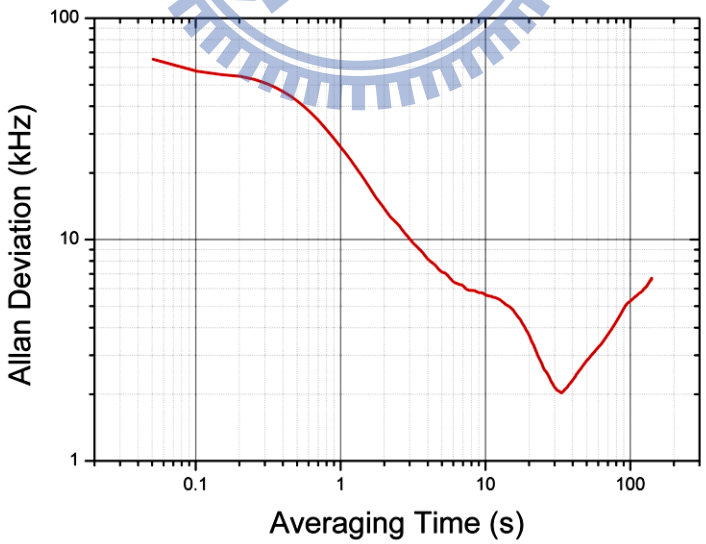

Fig. 5-4 Allan deviation of the laser locked to B2 component at 535 nm.

5.3.4 Absolute Frequency, Hyperfine Splitting and Center of Gravity of the Thallium $6P_{3/2} \rightarrow 7S_{1/2}$ Hyperfine Transitions

The absolute frequency measurements of the $6P_{3/2} \rightarrow 7S_{1/2}$ hyperfine transitions were performed using the HighFinesse wavelength meter, while the laser was locked to the zero-crossing points of the third derivative signal. Each measurement of the locked laser frequency was finished in 5 minutes after calibration of the wavelength meter. The accuracy of the wavelength meter was re-checked with the calibration laser after every measurement. The laser was unlocked and relocked between every measurement. More than 5000 data were taken for each individual measurement and more than 20 frequency measurements were taken for each of these four locked laser frequencies. The standard deviation for each frequency measurement of these four strong components was from 0.8 to 2.6 MHz, which depended on the SNR. The standard error of the mean, as the statistical uncertainty of the central frequency, of each hyperfine transition was from 8 to 18 kHz. Various systematic uncertainties were also studied, including: 0.6 MHz error due to the DC-offset of the third derivative signal and 0.2 MHz uncertainty caused by the electronic noise. However, the final accuracies of frequency measurements, which were dominated by the accuracy of the wavelength meter, were 30 MHz for all of the A1, A2, B1, and B2 components.

The signal amplitude of A3 and B3 components were too small to stabilize the laser for a direct frequency measurement. Alternatively, the frequency intervals A2-A3 and B2-B3 were acquired from the observed spectrum by scanning the laser frequency. The third derivative spectrum in Fig. 5-3, where the frequency axis was given by simultaneously acquiring the wavelength meter output, was obtained in a total measuring time of 10 min. Two crossover signals of A2, A3 and B2, B3 components could be also observed in the spectrum. In this method, two major systematic errors

must be taken care: the DC-offset of the signal and the determination of the zero-crossing point (the line center). The DC-offset of the third derivative signal was carefully removed before performing the frequency interval measurement. The zero-crossing point frequencies were determined using the cubic spline interpolation of the nearby data points. Data analysis for 12 upward and downward laser frequency scans gave the frequency intervals of 524.6(1.1) MHz and 531.64(50) MHz for A2-A3 and B2-B3 components, respectively. Our results agree very well with the best previous measurements [33]. With the measured absolute frequencies of A2 and B2 components, the absolute frequencies of A3 and B3 component were then derived from the A2-A3 and B2-B3 frequency intervals. Combining with the precise values of HFSs of $6P_{3/2}$ [33] and $7S_{1/2}$ [9], we were able to derive the center of gravity (c.g.) of the $6P_{3/2} \rightarrow 7S_{1/2}$ transition frequency with an accuracy of 17 MHz. The results of the absolute frequency measurements of the hyperfine components of ^{203}Tl and ^{205}Tl at 14 torr Ne background pressure are listed in Table 5-1. The IS of this transition was calculated to be 1757(24) MHz, which is consistent with the previous result [34], by subtracting the c.g. frequencies of the two isotopes.

The pressure shift of this transition under neon has been measured to be −2.3(1.0) MHz/torr [95]. Therefore, by taking the pressure shift (−33 ± 14 MHz) into account, the zero-pressure transition frequencies of the $6P_{3/2} \rightarrow 7S_{1/2}$ transition was determined to be 560 155 914(22) MHz and 560 157 671(22) MHz for ^{203}Tl and ^{205}Tl, respectively. The energy of the $6P_{3/2} \rightarrow 7S_{1/2}$ transition has been calculated to be 18619 cm^{-1}, corresponding to 558 183.6 GHz, using the many-body perturbation theory (MBPT) with the configuration interaction (CI) method [35].

Table 5-1. The absolute frequencies of the hyperfine components within $6P_{3/2} \rightarrow 7S_{1/2}$ transition of of ^{203}Tl and ^{205}Tl in HCL at a background neon pressure of 14 torr.

Line	F-F'	Frequency (MHz)
A1	^{203}Tl, 1-0	560 147 075 (30)
B1	^{205}Tl, 1-0	560 148 751 (30)
A2	^{203}Tl, 2-1	560 158 729 (30)
A3	^{203}Tl, 1-1	560 159 254 (30)
B2	^{205}Tl, 2-0	560 160 514 (30)
B3	^{205}Tl, 1-1	560 161 045 (30)
cg of ^{203}Tl	$6P_{3/2} \rightarrow 7S_{1/2}$	560 155 881 (30)
cg of ^{205}Tl	$6P_{3/2} \rightarrow 7S_{1/2}$	560 157 638 (30)
Experiment[94], ^{205}Tl	$6P_{3/2} \rightarrow 7S_{1/2}$	560 156.2 (GHz)
Theory [35] , ^{205}Tl	$6P_{3/2} \rightarrow 7S_{1/2}$	558 3.6 (GHz)

Chapter 6

Summary

6.1 Summary

A single frequency 1070 nm Nd:$GdVO_4$ laser has been demonstrated using a VBG as an output coupler in a plano-concave cavity. The VBG provides efficient mode selection to achieve single frequency operation. In comparison with our previous Fabry-Perot cavity laser [44], better output power and stability was obtained by using a plano-concave cavity to adapt the thermal focal length of the laser crystal. Output power of 300 mW was achieved at 3 W pump power, and the slope efficiency was 14.5%. The beam propagation parameter M^2 of this laser at 200 mW output power was ~ 1.2, indicating a good beam quality. The single frequency tuning range by changing cavity length was about 5.1 GHz at output power 100 mW. The tuning range can be greatly increased by simultaneously tuning the VBG while scan the PZT such that the reflection peak of VBG is coincide with the laser frequency. To demonstrate its application to spectroscopy, the laser was frequency locked to a confocal Fabry-Perot cavity and a relative stability of 7.58 kHz was obtained. A second generation of the 1070-nm laser adopted a new Nd:$GdVO_4$ laser crystal with spherical input surface has been setup to increase the frequency stability. After frequency doubling using PPLN, this laser is an excellent light source for thallium spectroscopy at 535 nm.

The frequency doubled 1070-nm Nd:$GdVO_4$ laser has been stabilized to the a_1, a_{10}, and a_{15} hyperfine transitions of P(28) 30-0 line of $^{127}I_2$ and their absolute frequencies were measured by an OFC. The pressure shift in the iodine cell was investigated to deduce the zero-pressure absolute frequency. The pressure broadening and power broadening effects were also investigated for the a_{10} hyperfine component. The P(28) 30-0 line of iodine is close to the $6P_{3/2}$-$7S_{1/2}$ transition of the thallium atom.

The saturated absorption spectrum of the hyperfine components of the $6P_{3/2} \rightarrow 7S_{1/2}$ transition of ^{203}Tl and ^{205}Tl in a hollow cathode lamp was also observed using the tunable frequency doubled 1070 nm Nd:$GdVO_4$ laser. The laser can be frequency stabilized to the four strong hyperfine components with a stability of 30 kHz at 1 s averaging time. Furthermore, the absolute frequencies of the hyperfine components was measured using a precision wavelength meter with accuracy of 30 MHz. Combining with previous accurate HFS of the $6P_{3/2}$ and $7S_{1/2}$, the c.g. of the transition frequency of $6P_{3/2} \rightarrow 7S_{1/2}$ was determined to an accuracy of 22 MHz (better than 4×10^{-8}) for both isotopes. Finally, the IS of $6P_{3/2} \rightarrow 7S_{1/2}$ transition determined was also in good agreement with the previous measurement. The results will serve as the experimental constraints and benchmarks for the improvements of thallium wavefunction calculations.

6.2 Future Works

To improve the frequency stability of the laser, a thermal isolated and stabilized reference cavity is needed to lock the laser. With a stable cavity to lock the laser, a PZT quick scanning ability of the laser will acquire a whole saturation spectrum in a short time to reduce the long term drift and frequency readings can be acquired from a fast wavelength meter simultaneously.

In the future, the developed compact 535 nm laser system with a power >50 mW and a frequency tuning range of 10 GHz will be used for the thallium laser cooling experiment. The PNC measurement in thallium using electromagnetically induced transparency (EIT) has been proposed to improve the PNC measurement [98] in which a 535 nm laser is required. This laser system will be employed to investigate the $6P_{3/2} \rightarrow 7S_{1/2}$ transition using a thallium hollow cathode lamp and the PNC effect using the EIT spectrum in atomic thallium.

References

1. C. S. Wood, S. C. Bennett, D. Cho, B. P. Masterson, J. Roberts, C. E. Tanner, and C. E. Wieman, "Measurement of Parity Nonconservation and an Anapole Moment in Cesium." Science **275**, 1759 (1997).
2. V. A. Dzuba, V. V. Flambaum, and J. S. M. Ginges, "High-precision calculation of parity nonconservation in cesium and test of the standard model" Phys. Rev. D **66**, 076013 (2002).
3. P. A. Vetter, D. M. Meekhof, P. K.Majumder, S. K. Lamoreaux, and E. N. Fortson, "Precise measurement of parity nonconserving optical rotation in atomic thallium," Phys. Rev. Lett. **74**, 2658 (1995).
4. N. H. Edwards, S. J. Phipp, P. E. G. Baird, and S. Nakayama, "Precise measurement of parity nonconserving optical rotation in atomic thallium," Phys. Rev. Lett. **74**, 2654 (1995).
5. B. C. Regan, E. D. Commins, C. J. Schmidt, and D. DeMille, "New limit on the electron electric dipole moment,"Phys. Rev. Lett. **88**, 071805 (2002).
6. J. J. Hudson, D. M. Kara, I. J. Smallman, B. E. Sauer, M. R. Tarbutt, and E. A. Hinds, "Improved measurement of the shape of the electron," Nature (London) **473**, 493 (2011).
7. I. Fan, T.-L. Chen, Y.-S. Liu, Y.-H. Lien, Y.W. Liu, "Prospects of laser cooling in atomic thallium," Phys. Rev. A **84**, 042504 (2011).
8. B. Kl¨oter, C.Weber, D. Haubrich, D. Meschede, and H. Metcalf, "Laser cooling of an indium atomic beam enabled by magnetic fields," Phys. Rev. A **77**, 033402 (2008).
9. T.-L. Chen, I. Fan, H.-C. Chen, C.-Y. Lin, S.-E. Chen, J.-T. Shy, and Y.-W. Liu, "Absolute frequency measurement of the $6P_{1/2} \rightarrow 7S_{1/2}$ transition in thallium," Phys. Rev. A **86**, 052524 (2012).
10. Y. F. Chen, M. L. Ku, and K. W. Su, "High-power efficient tunable Nd:$GdVO_4$ laser at 1083 nm ", Opt. Lett. **30**, 2107 (2005).
11. L. B. Glebov, "Volume Bragg gratings in PTR glass—new optical elements for laser design," in Advanced Solid State Photonics, OSA Technical Digest Series (CD) (Optical Society of America, 2008), paper MD1.
12. T. Y. Chung, A. Rapaport, V. Smirnov, L. B. Glebov, M. C. Richardson, and M.

Bass, “Solid-state laser spectral narrowing using a volumetric photothermal refractive Bragg grating cavity mirror,” Opt. Lett. **31**, 229 (2006).

13. B. Jacobsson, V. Pasiskevicius, and F. Laurell, “Single-longitudinal Nd-laser with a Bragg-grating Fabry-Perot cavity,” Opt. Express **14**, 9284 (2006).
14. T. J. Quinn, “Practical realization of the definition of the metre, including recommended radiations of other optical frequency standards (2001),” Metrologia **40**, 103 (2003).
15. R. Felder, “Practical realization of the definition of the metre, including recommended radiations of other optical frequency standards (2003),” Metrologia **42**, 323 (2005).
16. “IodineSpec5,” http://www.iqo.uni-hannover.de.
17. C.-C. Liao, K.-Y. Wu, Y.-H. Lien, H. Knöckel, H.-C. Chui, E. Tiemann, and J.-T. Shy, “Precise frequency measurements of $^{127}I_2$ lines in the wavelength region 750–780 nm,” J. Opt. Soc. Am. B **27**, 1208 (2010).
18. “HighFinesse product manual”, http://www.highfinesse.com/.
19. J. Beringer et al. (Particle Data Group), PR D**86**, 010001 (2012) and 2013 partial update for the 2014 edition (URL: http://pdg.lbl.gov)
20. M. Bouchiat and C. Bouchiat, “Parity violation in Atoms,” Rep. Prog. Phys. **60** 1351 (1997).
21. R. N. Cahn and F. J. Gilman, “Polarized electron-Nucleon Scattering in Gauge Theories of Weak and Electromagnetic Interactions ,“ Phys. Rev. D**17**, 1313 (1978).
22. M. J. Musolf, T. W. Donnelly, J. Dubach, S. J. Pollock, S. Kowalski, and E. J. Beise, “Intermediate-energy semileptonic probes of the hadronic neutral current,” Phys. Rept. **239**, 1 (1994).
23. Y. B. Zeldovich, “Parity nonconservation in the first order in the weak-interaction constant in electron scattering and other effects,” Sov. Phys. JETP **9**, 682 (1959).
24. M.-A. Bouchiat and C. Bouchiat, “Parity violation induced by weak neutral currents in atomic physics I,” J. de Physique **35,** 899 (1974).
25. E. N. Fortson and L. L. Lewis, “Atomic parity nonconservation experiments,” Phys. Rept. **113**, 289 (1984)
26. A. Derevianko and S.G. Porsev, “Theoretical overview of atomic parity violation,”

Eur. Phys. J. A **32**, 517 (2007)

27. M.J.D. Macpherson, K.P. Zetie, R.B. Warrington, D.N. Stacey, and J.P. Hoare, "Precise measurement of parity nonconserving optical rotation at 876 nm in atomic bismuth," Phys. Rev. Lett. **67**, 2784, 1991.
28. D.M. Meekhof, P. Vetter, P.K. Majumder, S.K. Lamoreaux, and E.N. Fortson. "High-precision measurement of parity nonconserving optical rotation in atomic lead," Phys. Rev. Lett. **71**, 3442 (1993).
29. D.M. Lucas, R.B. Warrington, D.N. Stacey, and C.D. Thompson, "Search for parity nonconserving optical rotation in atomic samarium," Phys. Rev. A **58**, 3457 (1998).
30. P. S. Drell and E. D. Commins, "Parity nonconservation in atomic thallium". Phys. Rev. Lett. **53**, 968 (1984).
31. K. Tsigutkin, D. Dounas-Frazer, A. Family, J.E. Stalnaker, V.V. Yashchuk, and D. Budker, "Observation of a large atomic parity violation effect in ytterbium," Phys. Rev. Lett. **10**, 071601 (2009).
32. A. Lurio and A. G. Prodell, "Hfs Separations and Hfs anomalies in the $^2P_{1/2}$ state of Ga^{69}, Ga^{71}, Tl^{203}, and Tl^{205}," Phys. Rev. **101**, 79 (1956).
33. G. Gould, "Hfs separations and hfs anomaly in the $6^2P_{3/2}$ metastable level of Tl^{203} and Tl^{205}," Phys. Rev. **101**, 1828 (1956).
34. G. Hermann, G. Lasnitschka, and D. Spengler, "Hyperfine structures and level isotope shifts of the $n^2S_{1/2}$ (n=7-12)-and $n^2D_{3/2,5/2}$(n=6-10)-levels of ^{203,205}Tl measured by atomic beam spectroscopy," Z. Phys. D 28, 127 (1993).
35. M. G. Kozlov, S. G. Porsev, and W. R. Johnson, "Parity nonconservation in thallium," Phys. Rev. A **64**, 052107 (2001).
36. M. S. Safronova, "Atomic calculations for tests of fundamental physics," Can. J. Phys. **89**, 371 (2011).
37. http://www.optigrate.com
38. B. L. Volodin, S. V. Dolgy, E. D. Melnik, E. Downs, J. Shaw, and V. S. Ban, "Wavelength stabilization and spectrum narrowing of high-power multimode laser diodes and arrays by use of volume Bragg gratings," Opt. Lett. **29**, 1891 (2004).
39. G. Venus, L. Glebov, V. Rotar, V. Smirnov, P. Crump, and J. Farmer, "Volume

Bragg semiconductor lasers with near diffraction limited divergence," Proc. SPIE **6216**, 621602 (2006).

40. B. Jacobsson, V. Pasiskevicius, and F. Laurell, "Tunable single-longitudinal-mode ErYb:glass laser locked by a bulk glass Bragg grating," Opt. Lett. **31**, 1663 (2006).
41. I. Häggström, B. Jacobsson, and F. Laurell, "Monolithic Bragg-locked Nd:$GdVO_4$ laser," Opt. Express **15**, 11589 (2007).
42. B. Jacobsson, J. E. Hellström, V. Pasiskevicius, and F. Laurell, "Widely tunable Yb:KYW laser with a volume Bragg grating," Opt. Express **15**, 1003 (2007).
43. J. E. Hellström, B. Jacobsson, V. Pasiskevicius, and F. Laurell, "Quasi-two-level Yb:KYW laser with a volume Bragg grating," Opt. Express **15**, 13930 (2007).
44. T.-Y. Chung, S. S. Yang, C.-W. Chen, H.-C. Yang, C.-R. Liao, Y.-H. Lien, and J.-T. Shy, "Wavelength tunable single mode Nd:$GdVO_4$ laser using a volume Bragg grating fold mirror," in Conference on Lasers and Electro-Optics/Quantum Electronics and Laser Science Conference and Photonic Applications Systems Technologies, OSA Technical Digest Series (CD) (Optical Society of America, 2007), paper CThE4.
45. B. Jacobsson, J. E. Hellström, V. Pasiskevicius, and F. Laurell, "Tunable Yb:KYW laser using volume Bragg grating in s-polarization," Appl. Phys. B **91**, 85 (2008).
46. T. H. Wang, Y. L. Ju, X. M. Duan, B. Q. Yao, X. T. Yang, and Y. Z. Wang, "Narrow linewidth continuous wave diode-pumped Tm:YLF laser with a volume Bragg grating," Laser Phys. Lett. **6**, 117 (2009).
47. N. Vorobiev, L. Glebov, and V. Smirnov, "Single-frequency-mode Q-switched Nd:YAG and Er:glass lasers controlled by volume Bragg gratings," Opt. Express **16**, 9199 (2008).
48. M. Hemmer, Y. Joly, L. B. Glebov, M. Bass, and M. C. Richardson, "Volume Bragg Grating assisted broadband tunability and spectral narrowing of Ti:sapphire oscillators," Opt. Express **17**, 8212 (2009).
49. M. Henriksson, M. Tiihonen, V. Pasiskevicius, and F. Laurell, "$ZnGeP_2$ parametric oscillator pumped by a linewidth-narrowed parametric 2 μm source," Opt. Lett. **31**, 1878 (2006).

50. J. Saikawa, M. Fujii, H. Ishizuki, and T. Taira, “52 mJ narrow-bandwidth degenerated optical parametric system with a large-aperture periodically poled MgO:$LiNbO_3$ device,” Opt. Lett. **31**, 3149 (2006).
51. J. Saikawa, M. Fujii, H. Ishizuki, and T. Taira, “High-energy, narrow-bandwidth periodically poled Mg-doped $LiNbO_3$ optical parametric oscillator with a volume Bragg grating,” Opt. Lett. **32**, 2996 (2007).
52. B. Jacobsson, C. Canalias, V. Pasiskevicius, and F. Laurell, “Narrowband and tunable ring optical parametric oscillator with a volume Bragg grating,” Opt. Lett. **32**, 3278 (2007).
53. P. Jelger and F. Laurell, “Efficient narrow-linewidth volume-Bragg grating-locked Nd:fiber laser,” Opt. Express **15**, 11336 (2007).
54. P. Jelger and F. Laurell, “Efficient skew-angle cladding-pumped tunable narrow-linewidth Yb-doped fiber laser,” Opt. Lett. **32**, 3501 (2007).
55. T. McComb, V. Sudesh, and M. Richardson, “Volume Bragg grating stabilized spectrally narrow Tm fiber laser,” Opt. Lett. **33**, 881 (2008).
56. J. W. Kim, P. Jelger, J. K. Sahu, F. Laurell, and W. A. Clarkson, “High-power and wavelength-tunable operation of an Er,Yb fiber laser using a volume Bragg grating,” Opt. Lett. **33**, 1204 (2008).
57. K. Seger, B. Jacobsson, V. Pasiskevicius, and F. Laurell, “Tunable Yb:KYW laser using a transversely chirped volume Bragg grating,” Opt. Express **17**, 2341 (2009).
58. B. Jacobsson, V. Pasiskevicius, F. Laurell, E. Rotari, V. Smirnov, and L. Glebov, “Tunable narrowband optical parametric oscillator using a transversely chirped Bragg grating,” Opt. Lett. **34**, 449 (2009).
59. D. R. Drachenberg, O. Andrusyak, G. Venus, V. Smirnov, J. Lumeau, and L.B. Glebov, “Ultimate efficiency of spectral beam combining by volume Bragg gratings,” Appl. Opt. **52**, 7233 (2013)
60. B. Jacobsson, “Spectral control of lasers and optical parametric oscillators with volume Bragg gratings,” PhD-thesis, Trita-FYS 2008:13, KTH, Stockholm, Sweden (2008).
61. I. V. Ciapurin, L. B. Glebov, and V. I. Smirnov, "Modeling of Gaussian beam diffraction on volume Bragg gratings in PTR glass," Proc. SPIE **5742**, 183

(2005).

62. I. V. Ciapurin, V. Smirnov, D. R. Drachenberg, G. B. Venus and L. B. Glebov, “Modeling of phase volume diffractive gratings, part 2: reflecting sinusoidal uniform gratings, Bragg mirrors,” Opt. Eng. **51**, 058001 (2012).
63. J. E. Hellström, B. Jacobsson, V. Pasiskevicius, and F. Laurell, “Finite beams in reflective volume Bragg gratings: theory and experiments,” IEEE J. of Quantum Electron. **44**, 81 (2008).
64. M. Henriksson, “Tandem optical parametric oscillators using volume Bragg grating spectral control,” PhD-thesis, TRITA-FYS 2010:21, KTH, Stockholm, Sweden (2010).
65. H. Kogelnik, “Coupled wave theory for thick hologram gratings,” Bell Syst. Tech. J. **48**, 2909 (1969).
66. P. Blau, S. Pearl, S. Fastig and R. Lavi, "Single-mode operation of a mid-infrared optical parametric oscillator using volume-Bragg-grating cavity mirrors," IEEE J. Quant. Elec. **44**, 867 (2008).
67. A. J. Merriam, V. Smirnov, and L. Glebov, “Spectral narrowing and tenability of a high-power diffraction-limited ns-pulsed OPO/OPA system using transversely-chirped and temperature-tuned volume Bragg gratings,” Proc. SPIE **7193**, 71930R (2009).
68. S. Santran, M. Martinez-Rosas “Nonlinear refractive index of photo-thermo-refractive glass”, Optical Materials **28**, 401 (2006)
69. I. V. Ciapurin, V. Smirnov, D. R. Drachenberg, G. B. Venus and L. B. Glebov, “Modeling of phase volume diffractive gratings, part 2: reflecting sinusoidal uniform gratings, Bragg mirrors,” Opt. Eng. **51**, 058001 (2012).
70. Chien-Jung Liao, “Studies of single mode Nd:$GdVO_4$ laser,” Master thesis, NTHU, 2007.
71. T.Y. Chung, C.J.Liao1, Y. H. Lien, S .S. Yang, and J. T. Shy, “Special laser wavelength generation using a volume Bragg grating as Nd:$GdVO_4$ laser mirror,” Jpn. J. Appl. Phys. **49**, 062503 (2010)
72. Y. Sato and T Taira, “Comparative study on the spectroscopic properties of Nd:$GdVO_4$ and Nd:YVO_4 with hybrid process” IEEE J. Sel. Top. Quantum Electron. **11**, 613 (2005).

73. A. I. Zagumennyi, V. G. Ostroumov, I. A. Shcherbarkov, T. Jensen, J. P. Meyn, and G. Huber, "The Nd:$GdVO_4$ crystal: a new material for diode-pumped lasers," Sov. J. Quantum Electron. **22**, 1071 (1992).
74. H. D. Jiang, H. J. Zhang, J. Y. Wang, H. R. Xia, X. B. Hu, B. Teng, C. Q. Zhang, "Optical and laser properties of Nd:$GdVO_4$ crystal," Opt. Commun. **198**, 447 (2001).
75. M. Liao, 1 R. Lan, Z. Wang, H. Zhang, J. Wang, X. Hou, and X. Xu, "10 W continuous-wave Nd:$GdVO_4$ microchip laser", Laser Phys. Lett. **5**, 503 (2008)
76. I. Velchev, W. Hogervorst, and W. Ubachs, "Precision VUV spectroscopy of Ar I at 105 nm," J. Phys. B: At. Mol. Opt. Phys. **32**, L511 (1999).
77. S. L. Cornish, Y.-W. Liu, I. C. Lane, P. E. G. Baird, G. P. Barwood, P. Taylor, and W. R. C. Rowley, "Interferometric measurements of $^{127}I_2$ reference frequencies for 1S–2S spectroscopy in muonium, hydrogen, and deuterium," J. Opt. Soc. Am. B **17**, 6 (2000).
78. P. Cancio Pastor, G. Giusfredi, P. De Natale, G. Hagel, C. de Mauro, and M. Inguscio, "Absolute frequency measurements of the $2^3S_1 \rightarrow 2^3P_{0,1,2}$ atomic helium transitions around 1083 nm," Phys. Rev. Lett. **92**, 023001 (2004).
79. S. Reinhardt, G.Saathoff, H. Buhr, L.A. Carlson, A. Wolf, D. Schwalm, S. Karpuk, C. Novotny, G. Huber, M. Zimmermann, R. Holzwarth, T. Udem, T.W. Hänsch, and G. Gwinner, "Test of relativistic time dilation with fast optical atomic clocks at different velocities," Nature Phys. **3**, 861 (2007).
80. Y.-C. Huang, W.-J. Luo, Y.-T. Kuo, and L.-B. Wang, "Precision measurement of hyperfine intervals in the D1 lines of atomic ^{7}Li," J. Phys. B: At. Mol. Opt. Phys. **46**, 075004 (2013).
81. A. Arie and R. L. Byer, "Laser heterodyne spectroscopy of $^{127}I_2$ hyperfine structure near 532 nm," J. Opt. Soc. Am. B **10**, 1990 (1993).
82. P. A. Jungner, S. Swartz, M. Eickhoff, J. Ye, J. L. Hall, and S. Waltman, "Absolute frequency of the molecular iodine transition R(56)32–0 near 532nm," IEEE Trans. Instrum. Meas. **44**, 151 (1995).
83. J. Ye, L. Robertsson, S. Picard, L. -S. Ma, and J. L. Hall, "Absolute frequency atlas of molecular I_2 lines at 532 nm," IEEE Trans. Instrum. Meas. **48**, 544 (1999).

84. G. Galzerano, C. Svelto, E. Bava, and F. Bertinetto, "High frequency-stability diode-pumped Nd:YAG lasers with the FM sidebands method and Doppler-free iodine lines at 532 nm," Appl. Opt. **38**, 6962 (1999).
85. F.-L. Hong and J. Ishikawa, "Hyperfine structures of the R (122)35-0 and P(84)33-0 transitions of $^{127}I_2$ near 532nm," Opt. Commun. **183**, 101 (2000).
86. L. J. Gillespie and L. H. D. Fraser, "The normal vapor pressure of crystalline iodine," J. Am. Chem. Soc. **58**, 2260 (1936)
87. H.-M. Fang, S. C. Wang, and J.-T. Shy, "Pressure and power broadening of the *a10* component of R(56)32–0 transition of molecular iodine at 532 nm," Opt. Commun. **257**, 76 (2006).
88. V.S. Letokhov, V.P. Chebotayev, Nonlinear Laser Spectroscopy, Springer, Berlin, 1977, pp. 72-80
89. N. Taylor, N. Omenetto, B. W. Smith, and J. D. Winefordner, "Measurement of number density of lead and thallium see-through hollow cathode discharges with a high resolution Fabry–Perot spectrometer and by conventional atomic absorption," Appl. Phys. B **89**, 99 (2007).
90. J.-T. Shy and T.-C. Yen, "Optogalvanic Lamb-dip frequency stabilization of a CO2 laser," Opt. Lett. **12**, 325 (1987).
91. P. V. K. Kumar and M. V. Suryanarayana, "Measurement of the hyperfine splitting of the 9 $S_{1/2}$ level in Cesium by Doppler-free two-photon spectroscopy," Opt. Commun. **285**, 1838 (2012).
92. P. V. Kiran Kumar, M. Sankari, and M. V. Suryanarayana, "Hyperfine structure of the $7d\ ^2D_{3/2}$ level in cesium measured by Doppler-free two-photon spectroscopy," Phys. Rev. A **87**, 012503 (2013).
93. M. Nakazawa, "Phase-sensitive detection on Lorentzian line shape and its application to frequency stabilization of lasers," J. Appl. Phys. **59**, 2297 (1986).
94. R. L. Kurucz, "Atomic spectral line database", http://cfawww.harvard.edu/amp/ampdata/kurucz23/sekur.html.
95. R. S. Qygdata, R. Bobkowski, E. Lisicki, and J. Szudy, "Pressure effects of neon and argon on the 535 nm thallium line," Z, Naturforsch. A **42**, 559 (1987).
96. http://www.optical-components.com/crystals.html
97. A I. Zagumennyi,Y D. Zavartsev, P. A. Studenikin, I. A. Shcherbakov, A. F.

Umyskov, "$GdVO_4$ crystals with Nd^{3+}, Tm^{3+}, Ho^{3+}, and Er^{3+} ions for diode-pumped microchip laser", *Proc. SPIE* **2698**, 182 (1996).

98. A. D. Cronin, R. B. Warrington, S. K. Lamoreaux, and E. N. Fortson, “Studies of electromagnetically induced transparency in thallium vapor and possible utility for measuring atomic parity nonconservation,” Phys. Rev. Lett. **80**, 3719 (1998).